PHOTOELECTRON IMAGING OF MOLECULAR ANIONS

by

Adam Wallace

A Dissertation Submitted to the Faculty of the

DEPARTMENT OF PHYSICS

In Partial Fulfillment of the Requirements

For the Degree of

DOCTOR OF PHILOSOPHY

In the Graduate College of

THE UNIVERSITY OF ARIZONA

2020

THE UNIVERSITY OF ARIZONA
GRADUATE COLLEGE

As members of the Dissertation Committee, we certify that we have read the dissertation
prepared by: Adam Wallace
titled:

and recommend that it be accepted as fulfilling the dissertation requirement for the Degree of Doctor of Philosophy.

Andrei Sanov Date: Aug 24, 2020

Oliver L.A. Monti Date: Aug 24, 2020

Michael F. Brown Date: Aug 25, 2020

Arvinder Sandhu Date: Aug 24, 2020

Charles A. Stafford Date: Aug 25, 2020

Final approval and acceptance of this dissertation is contingent upon the candidate's submission of the final copies of the dissertation to the Graduate College.

I hereby certify that I have read this dissertation prepared under my direction and recommend that it be accepted as fulfilling the dissertation requirement.

Date: Aug 24, 2020

Andrei Sanov
Chemistry and Biochemistry; Physics

ACKNOWLEDGEMENTS

I would like to thank my research advisor, Professor Andrei Sanov for his help, instruction, patience, enthusiasm and wonderful teaching style. I am a better researcher and person for having worked with him. Thank you to Dr. Lori Culberson and Dr. Dimitry Khuseynov for being inspiring mentors and for all the things you taught me about using the instrument and scientific process. Thank you to Dr. Andrew Dixon for many interesting conversations and your example of diligence. A special thanks goes to Dr. Christopher Blackstone for sharing this graduate experience with me. Our many discussions on science, life, instrumental problems and everything in between have made this stay much more enjoyable. I am glad to have worked with you for so long, though a little shorter would have been ok with both of us. Thanks to Yerbolat Dauletyarov and Beverly Ru for being supportive and helpful.

Thanks to Justin Klaus and Kevin Bao for their frequent help in keeping the instrument working and for helping me to make instrumental improvements.

Thanks to my dissertation committee, Professors Andrei Sanov, Oliver Monti, Michael Brown, Arvinder Sandhu, and Charles Stafford for your feedback.

I appreciate the support of University of Arizona, the Technology and Research Initiative Fund in Imaging and Photonics and the National Science Foundation.

Finally, thanks to family and friends for their support and encouragement, most especially my wonderful wife Megan and my three boys, Seth, Jared and Caleb. I could not have done this without you.

DEDICATION

To my family for their constant love and support though the good time and bad. This was made possible because of you.

TABLE OF CONTENTS

CHAPTER 1

CHAPTER 2:

CHAPTER 3:

CHAPTER 4:

CHAPTER 5:

LIST OF FIGURES

LIST OF TABLES

ABSTRACT

This dissertation employs photoelectron imaging spectroscopy to explore properties of molecular electronic structure of heterocyclic aromatics. First, photoelectron angular distributions of these molecules are modeled to gain insight into their stability and electronic structure. The model is adapted to include the local charge density of anionic aromatics and find trends in photoelectron angular distributions. Applications of this model may have the power to predict photoelectron angular distributions from *ab initio* calculations. Second, a photoelectron imaging study of three anion isomers of deprotonated isoxazole is presented. Deprotonation at the most acidic position yields the isoxazolide anion, but the reaction at another site cleaves the O-N bond and opens the ring of the anion. This bond breaking causes a rearrangement of the energies of its electronic states. The sensitivity of these competing deprotonation pathways is explored by adjustments made to ion generation conditions. Third, a study of bond-breaking probes a covalent bond stretched far beyond its equilibrium length. This transient structure has an inherently multiconfigurational electronic structure due to the interaction of two unpaired electrons−a diradical−over the distance of a few angstroms. This is achieved by attaching an electron to isoxazole which populates an antibonding orbital and cleaves the O-N bond. Photodetachment of this electron leave the molecule as a diradical with the molecular framework holding the two radical centers at a chemically relevant distance. Quantum calculations help to distinguish and assign the nearly degenerate electronic states in this *almost bonded* aromatic molecule. Ideas for future study are presented in the final chapter.

CHAPTER 1: INTRODUCTION

The fundamental physics and chemistry of a molecule's connectivity, stability, and reactivity are defined by its electronic structure. Electron interactions drive chemical bonding and reactions. As we break or form chemical bonds, the electronic structure gives insight into the intramolecular forces that hold molecules together. These interactions are crucial to chemistry, as they define the properties of not only stable molecules, but also very short-lived, unstable, or transient states.

In this work we focus on the heterocyclic aromatic molecules as a framework for understanding the strength of through-space intramolecular interactions and dependence of electronic structure on hetero atom substitution. We probe these fundamental properties through photoelectron imaging spectroscopy, which simultaneously provides energetic and structural information about unstable and transient neutral structures and their parent anions.

This introduction is divided into three parts, which set up the background information for the experimental and theoretical studies in this dissertation. First, we explore the chemical and physical problems we can study with heterocyclic aromatics and discuss what is known about their chemistry. Second, we outline the photoelectron imaging spectroscopy as the primary tool we use in these experiments. Lastly, we detail the analysis of photoelectron angular distributions and discuss the models used to probe electronic structure.

1.1 Heterocyclic Aromatic and Radical Chemistry

Aromatic molecules have cyclic, planar structures with a delocalized conjugated π system from alternating single and double bonds.[1,2] The resonance from these alternating bonds stabilizes the molecule making it less reactive. Heterocyclic aromatics have one or more of the carbons substituted for another element, which lowers the aromaticity and thus the stability. Heterocyclic aromatics are frequently used in organic synthesis, pharmaceutical production, pesticides, synthetic fuels and much more.[3-6]

In this work, we use heterocyclic aromatics because of their electronic structure and how that structure reacts to the addition of an electron or the removal of a proton. Several heterocyclic aromatic molecules experience bond fission upon electron attachment leaving the molecule with an unpaired electron as a radical anion.[7,8] The extra electron prevents the ring from closing again and stabilizes the molecule. This electron can then be photodetached creating a diradical, with the unpaired electrons largely localized near on the previously bonded atoms. The intact structure of the remaining ring allows us to study interaction of the two radical centers (i) through space, across a few angstroms gap resulting from the bond dissociation, and (ii) through the rest of the chemical bonds forming the ring-open molecular skeleton.

Deprotonation of heterocyclic aromatics also initiates interesting chemical interactions. Due to their heterocyclic nature, these molecules typically have several non-equivalent deprotonation sites. A deprotonation reaction at each of these sites yields a distinct anion isomer. Although these anions inherit the closed-shell electron configuration of the parent stable molecules, they often open pathways to more complex structures,[3,9] many of which have not been studied. In particular, some heterocyclic aromatics have been shown to undergo bond fission or fragmentation upon electron capture.[10,11] Negative ion photoelectron imaging spectroscopy provides access to many metastable or unstable neutral or anionic states. The goal of this dissertation is to study bond breaking events in heterocyclic aromatics and better understand their electronic structure.

1.2 Negative Ion Photoelectron Imaging Spectroscopy

Negative ion photoelectron spectroscopy is performed by photodetaching an electron from an anion with a photon of known energy. For the electron to be ejected, the photon energy must be sufficiently large to overcome the binding energy for that electron. We are then left with a neutral molecule and a free electron ejected into the continuum of energy states. By the conservation of energy, the photon energy must be equal to the sum of the electron kinetic energy (eKE) and the electron binding energy (eBE).[12]

$$h\nu = \mathrm{eKE} + \mathrm{eBE}. \tag{1.1}$$

By using monochromatic light, a measurement of eKE determines the eBE. Because the anion is in its ground state this gives the entire spectrum of vibrational and electronic energy states of the neutral molecule for which we have enough energy to access as shown in Figure 1.2.[13]

Using negative ions for photoelectron spectroscopy has some benefits over neutral molecules. The additional electron in an anion is more weakly bound than the electrons of a neutral molecule. This allows for the use of visible or near-UV light for photodetachment from table-top laser sources as opposed to x-ray radiation needed for photoionization. After an electron is photodetached from an anion it interacts with the remaining neutral core. This interaction is quite weak compared to photoionization where the core and the outgoing

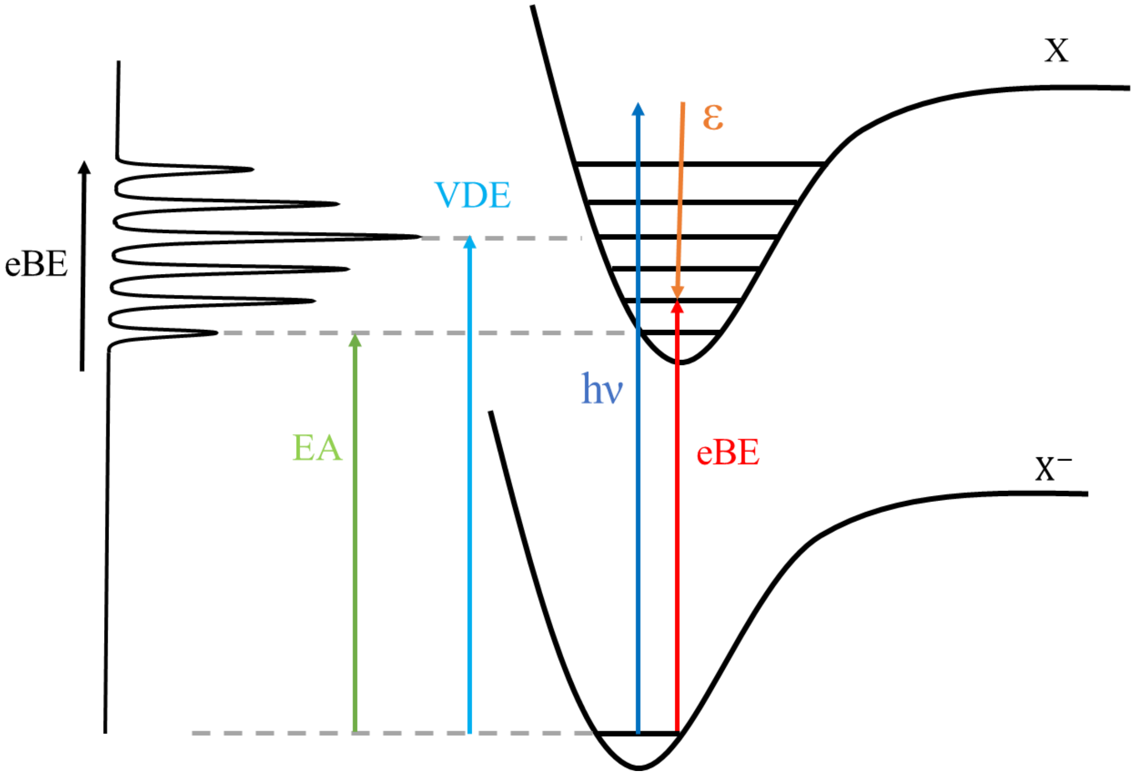

Figure 1.1 Schematic of photoelectron spectroscopy. An anion in its ground electronic and vibrational states absorbs a photon of energy $h\nu$ (blue), which photodetaches an electron. The resulting electron is ejected with a kinetic energy of ε (orange) corresponding to the difference between the photon energy and electron binding energy (eBE, red). $h\nu = \text{eBE} + \varepsilon$. The vertical detachment energy (VDE, light blue) corresponds to the energy gap between the anion ground state and the vibrational state of the neutral with the greatest Frank-Condon overlap with the vibrational state of the anion. The adiabatic electron affinity (EA, green) corresponds to detachment to the ground vibrational state of the neutral. The photoelectron energy spectrum corresponding to these transitions is given on the left.

electron are both charged, which simplifies the analysis for anion photodetachment.[14] Additionally, charged molecules can be easily isolated in the gas phase by their mass to charge ratio using a time-of-flight mass spectrometer (TOF-MS). Most importantly, using anions allows access very short-lived or unstable neutral states as long as there exists a stable anion state.

Photodetached electrons interact with the electric field of the laser and are ejected in preferential directions relative to that vector. The photoelectron angular distribution (PAD) reflects the symmetry of the parent orbital from which the electron was emitted.[15,16] Analysis of PADs can help in spectral assignments or even help to resolve some nearly degenerate energy states. One of the greatest strengths of photoelectron imaging is the ability to simultaneously capture the photoelectron energy spectrum and the angular distribution.

The first two-dimensional imaging experiments were designed in 1987[17] by Chandler and Houston to study photofragments and the technique was later expanded to study photoelectrons. Ten years later, the resolution of these experiments was drastically improved by the introduction of velocity map imaging,[18,19] which focuses all photoelectrons with the same velocity vector onto the same position of a 2-dimentional detector. In the early 2000s photoelectron imaging began to be applied to negative ions.[20,21] Over the last few years models have been developed to describe the relationship between PADs and the molecular orbitals of parent anion from which the anion was ejected.[22,23]

1.3 Modeling of Photoelectron Angular Distributions

Photoemitted electrons carry information about the electronic states of both the parent anion and resulting neutral molecule[15,16]. The photoelectron angular distribution (PAD) results from the interaction with the laser polarization and reflects the properties of the molecular orbitals of the anion from which the electron was emitted. The PAD for an electron emitted by single linearly polarized light is described by[24]

$$I(\theta) = \frac{\sigma}{4\pi}[1 + \beta P_2(\cos\theta)] \tag{1.2}$$

where I(θ) is the PAD, θ is the angle between the laser polarization and the photoelectron velocity vector, σ is the total photodetachment cross-section, β is the anisotropy parameter, and $P_2(\cos\theta) = (1/2)(3\cos^2\theta - 1)$ is the second-order Legendre polynomial. I(θ) is always a positive number which means β ranges from -1 for purely perpendicular transition to 2 for purely parallel transitions.

In the case of photodetachment from an atomic anion, the initial state of the electron can be described by the orbital angular momentum quantum number, *l*. A photon carries a single unit of angular momentum, which it imparts upon the electron creating an outgoing photoelectron wave represented by the superposition of partial waves with angular momentum quantum numbers $l \pm 1$. The result of this is a PAD with the anisotropy parameter described by the Cooper-Zare central-potential formula derived by Bethe[25], and generalized by Cooper and Zare[26,27]:

$$\beta_l = \frac{l(l-1)\chi_{l,l-1}^2 + (l+1)(l+2)\chi_{l,l+1}^2 - 6l(l+1)\chi_{l,l+1}\chi_{l,l-1}\cos(\delta_{l+1,l-1})}{(2l+1)[l\chi_{l,l-1}^2 + (l+1)\chi_{l,l+1}^2]} \tag{1.3}$$

In this equation $\chi_{l,l\pm1}$ are the magnitudes of the radial transition dipole matrix elements for the $l \pm 1$ partial wave emitted from the atomic orbital with angular momentum quantum number *l*, and $\delta_{l+1,l-1}$is the phase shift induced by the interaction of the partial waves with the remaining neutral atom.

Evaluation of the transition dipole matrix elements $\chi_{l,l\pm1}$ can be very challenging. Hanstorp *et al.* proposed an alternative approach[14] by assuming the relative scaling of the partial wave cross-sections, and thus the transition dipole moment elements, follow the Wigner Threshold Law[28]. This allows us to express the ratio of the transition dipole moment elements to be proportional to the electron kinetic energy[14,28]

$$\chi_{l,l+1}/\chi_{l,l-1} = \mathrm{A}_l\varepsilon \tag{1.4}$$

where A_l is a proportionality constant and ε is electron kinetic energy. The Cooper-Zare formula can be rearranged to express β_l in terms of this ratio $\chi_{l,l+1}/\chi_{l,l-1}$ and simplified to allow the calculation of β_l as a function of $\varepsilon \equiv$ eKE:

$$\beta_l(\varepsilon) = \frac{l(l-1)+(l+1)(l+2)A_l^2\varepsilon^2-6l(l+1)A_l\varepsilon\cos(\delta_{l+1,l-1})}{(2l+1)[l+(l+1)A_l^2\varepsilon^2]}\,. \tag{1.5}$$

Even with the Hanstorp approximation, the Cooper-Zare formula can only be used to describe emission from atomic orbitals.[29] However, there are some molecular orbitals that can be approximated by atomic orbitals. For example, the π_g^* HOMO of O_2^- closely resembles an atomic d-orbital and it can be modeled well by Equation 1.5 with *l*=2[30-32]. Most molecular systems have orbitals that are considerably more complicated than atomic orbitals and thus the Cooper-Zare formula is insufficient to model their PADs.

Many molecular orbitals can be approximated by a linear combination of atomic orbitals, including the common class of sp^x hybrid orbitals. This motivated the formulation of a mixed-character model by our group to express the PAD for s-p hybridized orbitals.[22] The s-p model applies the same underlying principles as the Cooper-Zare formula applying the central-atom approximation, which considers the s and p functions to be localized in a single location in the parent anion.

The s-p model was first applied to solvated H^- and NH_2^- anions,[33] where the parent anions can be well described by *s* and *p* orbitals, respectively, and the solvation adds in a perturbation, breaking the wavefunction's symmetry. In the first case, this solvated cluster was described by a diffuse 2*p* orbital added (as a polarization/perturbation term) to the 1*s* orbital of H^-. For solvated NH_2^-, a diffuse 1*s* term was added to the anion's 2*p* orbital to account for the solvation-induced distortion of the parent orbital, resulting in the breaking of its odd character. In these initial studies, the change in character of the parent orbitals was small and therefore could be modelled as a perturbation of the isolated anion's state. However, it was noted that the derivation of the mixed *s*-*p* model did not make any assumptions about the relative amplitudes of the *s* and *p* components of the model function, meaning that the model itself was not perturbative in nature and could be applied to any mixed *s*-*p* state, regardless of the relative amplitudes of the *s* and *p* contributions. This realization prompted the next application of the model to systems with sp^x hybrid orbitals,[34,35] which are particularly ubiquitous in aromatic and heterocyclic compound.

Similar to the way the Cooper-Zare formula works for atoms, the s-p model describes the PAD for detachment from sp^x hybrid orbitals by using the following formula to describe the anisotropy parameter as a function of eKE[22,36]:

$$\beta_{sp}(\varepsilon) = \frac{2(1-\gamma_p)B_1\varepsilon + 2\gamma_p A_1^2\varepsilon^2 - 4\gamma_p A_1 \varepsilon \cos(\delta_2 - \delta_0)}{\gamma_p + 2\gamma_p A_1^2 \varepsilon^2 + (1-\gamma_p)B_1\varepsilon} \tag{1.6}$$

where A_1 is given by Eq. 1.4 with $l = 1$, γ_p is the fractional p-character of the parent anion:

$$|\,\psi_{sp}\rangle = \sqrt{1-\gamma_p}\,|\,s\rangle + \sqrt{\gamma_p}\,|\,p\rangle, \tag{1.7}$$

and B_1 is the relative scaling of the $s \rightarrow p$ and $p \rightarrow s$ photodetachment channels, defined by:

$$B_1\varepsilon = \frac{\chi_{0,1}^2}{\chi_{1,0}^2}. \qquad (1.8)$$

This model's application has allowed for the characterization of aromaticity and fractional hybridization of several heterocyclic aromatics and allowed for the assignment of multiple electronic states in convoluted spectra.

1.4 Conspectus of the Dissertation

In the following chapters of this dissertation, I present experimental and theoretical studies on the electronic structure of heterocyclic aromatics to expand models of photoelectron angular distributions and give insight into fundamental physical and chemical problems.

In Chapter 2, the experimental techniques and instrumentation are detailed. The chemistry of ion generation and the means of selecting ions of interest are explained. The use of laser systems is outlined along with typical operating procedures. Details are also given on data reduction and analysis.

Chapter 3 introduces the models that have been used to describe PADs and serval applications of those models. The models are expanded to describe local electron charge density at the deprotonation site. Comparisons are drawn between the models to discover trends and relate results of *ab initio* calculations to experimental results.

In Chapter 4, the chemistry of the deprotonated isoxazolide anion are explained. Several isomers due to deprotonation are presented along with some significant changes to molecular and electronic structure including the breaking of the aromatic ring. The photoelectron images and energy spectra are given, and electronic states of the corresponding neutrals are assigned.

Chapter 5 presents the results of a photoelectron imaging study of ring-opening in isoxazole. The interactions of two unpaired electrons over several angstroms act as an ‘almost formed’ chemical bond. This transient structure contains several nearly degenerate states including a ground state that is stretched far from its equilibrium geometry. Comparisons are made to the similar ring-opening in oxazole which produced a significantly more congested spectrum.

The dissertation concludes in chapter 6 with a summary and ideas for future photoelectron imaging studies.

CHAPTER 2: INSTRUMENTATION AND EXPERIMENTAL DESIGN

The experiments described here were performed on one of two similar custom-built photoelectron imaging spectrometers hereafter labeled as the east[37] and west instruments based on their location in the laboratory. The west instrument has been described elsewhere in detail[38] and is comprised of four primary regions of interest: the ion source chamber, the Wiley-McLauren time-of-flight mass spectrometer,[39,40] the velocity map imaging assembly[18,19,41] and the reflectron mass-spectrometer.

In the source chamber, ions are produced by intersection of a gas jet with an electron beam[42] and cooled in a supersonic expansion. The anions are then repelled down the time-of-flight mass spectrometer where they separate based on mass and the ion of interest is intersected spatially and temporally with a pulsed laser. Photoelectron imaging is performed by the velocity-map imaging[18,19,41] (VMI) assembly projecting emitted electrons onto a position sensitive detector. The reflectron is used to determine the mass of possible fragments formed by the laser-ion interaction. The entire instrument is held at varying levels of high vacuum by differential pumping. A schematic of the west instrument is given in figure 2.1. The east instrument is functionally similar, but without a reflectron and a few other differences that will be described later.

2.1 Vacuum System

The instruments are split into three differentially pumped sections each held at different pressures as illustrated in Figure 2.1. Under typical operating conditions (with the source

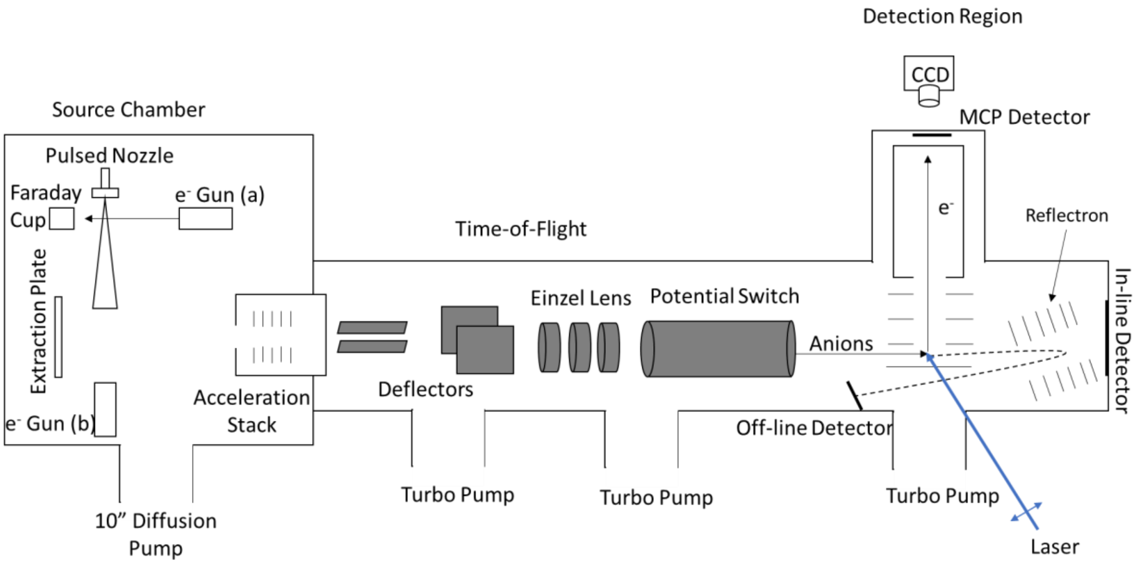

Figure 2.1 A schematic diagram of the photoelectron imaging spectrometer used in this work. The experiments were run with the electron gun in two different configurations, labeled (a) and (b). In (a) the electron gun or cannon sprayed electrons perpendicular to the expansion from the nozzle. The Faraday cup catches the high energy electrons and can be connected to an ammeter to measure electron current. Only an electron gun can be used in location (b), because the diffuse output of electrons from a cannon would not have sufficient concentration upon reaching the nozzle. The electron gun in (b) focuses a beam of electrons into the face of the nozzle which can act as a Faraday cup.

nozzle turned off), the source chamber is held at roughly 2-5 × 10^{-7} Torr by a Varian VHS-10 diffusion pump (5300 l/s), which is water cooled and backed by an Edwards E2M40 rotary pump (~14 l/s). A pneumatic gate valve (Vacuum Research Ltd model LP10) separates the diffusion pump from the source chamber when the instrument is not in use and the diffusion pump is turned off.

The source chamber is connected to the TOF region through a 4 mm aperture. This region is typically held at 1-4 × 10^{-7} Torr by two adjacent turbo pumps (Leybold, Turbovac 361, ~400 l/s) both of which are water cooled and backed in parallel by a single rotary pump (Leybold, Trivac D16B rotary pump, ~5.3 l/s). These pumps remain running even when the instrument is not in use. The two rotary pumps are used together to pump out the source chamber and TOF region after they have been vented to atmosphere. A 4” pneumatic gate valve is used to separate the TOF region from the detection region, which comprises both the VMI stack and the reflectron.

The detection region is typically held at 1-3 × 10^{-8} Torr by a third Leybold, Turbovac 361 turbomolecular pump backed by a Leybold, Trivac D16B rotary pump. This region may be vented to atmosphere for repairs separate from the rest of the instrument directly through the backing line for the turbo pump after the region has been pressurized with nitrogen. The rotary pump is then used to pump out the region to 2-3 × 10^{-4} Torr before the turbo pump can be reengaged.

When experiments are being performed (with the source supersonic nozzle running) the pressure of the source chamber, TOF region and detection region rise to 1-5 × 10^{-5}, 3-6 × 10^{-7}, and 2-5 × 10^{-8} Torr respectively. If the detection region reaches higher pressures, it can be baked by wrapping the outside of the instrument in heating tape overnight to encourage outgassing. This is particularly useful in the humid summer months if the detection region has been opened.

Each of the turbo pumps and the diffusion pump are water-cooled using a Neslab System 3 closed-loop liquid-to-liquid heat exchanger.

2.2 Ion Formation

Ions are generated via supersonic expansion of a precursor gas intersected by a high energy electron beam. The precursor gas is comprised of a carrier gas, typically Ar, CO_2, N_2O, or O_2, flowed over a sample in a stainless-steel tube outside the source chamber. The vapors from the sample are carried by the carrier gas out a pulsed nozzle (Parker, General Valve Series 9) in a supersonic expansion. Backing pressures of the carrier gas range from 10-30 psi gauge pressure depending on the gas. An IOTA ONE high speed valve driver (Parker Hannifin Co., General Valve) pulses a square wave 150-300 µs wide to open the solenoid-driven poppet at 20 or 50 Hz depending on the laser system in use. The supersonic expansion is then intersected 5-25 mm away from the nozzle by either a high energy (1keV) focused electron beam from an electron gun or a diffuse spray of 0.1 – 0.5 keV electrons from an electron "cannon." The electron gun and cannon arrangements and configurations are described in detail in subsection 2.2.1.

The high energy electrons ionize the supersonic expansion, creating a plasma and ejecting slower electrons.[42] These low-energy secondary electrons can then attach to neutral molecules or atoms in the supersonic expansion to produce metastable anions initiating various chemical reactions to form the anions of interest. The anions can be stabilized by collisions (eq. 2.1), dissociative attachment (eq. 2.2) or evaporative cooling (eq 2.3) of clusters[42-45]:

$$\mathrm{X} + e^- + \mathrm{Y} \rightarrow \mathrm{X}^{-^*} + \mathrm{Y} \rightarrow \mathrm{X}^- + \mathrm{Y}^* \qquad (2.1)$$

$$(\mathrm{XY}) + e^- \rightarrow (\mathrm{XY})^{-^*} \rightarrow \mathrm{X} + \mathrm{Y}^- \qquad (2.2)$$

$$\mathrm{X}_n + e^- \rightarrow [\mathrm{X}_n]^{-^*} \rightarrow [\mathrm{X}_{n-m}]^- + m\mathrm{X} \qquad (2.3)$$

In the presence of O^- radical anion, further anion chemistry can occur due to deprotonation (eq 2.4) or H_2^+ abstraction (eq 2.5).

$$\mathrm{HX} + \mathrm{O}^- \rightarrow \mathrm{X}^- + \mathrm{HO}^\bullet \qquad (2.4)$$

$$\mathrm{H_2X} + \mathrm{O}^- \rightarrow \mathrm{X}^- + \mathrm{H_2O} \qquad (2.5)$$

This method of ion generation produces high ion density (~$10^9/\mathrm{cm}^3$) with little loss, which allows for reactive anion formations via low-energy neutral-ion collisions.

Ion production from a neutral precursor is heavily dependent upon the vapor pressure of the liquid or solid sample. With some samples, ion production was low enough to be nearly undetectable. Two methods were employed to increase ion population for these samples: heating of the sample to ~40 C° and installing a newly designed sample holder to increase the amount of sample picked up by the carrier gas. The two types of sample holders are shown in Figure 2.2. The U-shaped sample holder increased the amount of sample ejected from the nozzle at the cost of more sample being consumed. For samples with high vapor pressure this sample holder is not needed, but it makes it possible to use low-vapor pressure samples. Care must be taken to ensure the pressure behind the nozzle is the same as in the sample holder else the sample could be pushed out of the nozzle all at once rather than just the vapors. This is achieved by using the empty top U-shaped tube to fill the backing line with carrier gas, creating equal pressures on both sides of the sample holder.

2.2.1 Electron Sources

The electron guns and cannons used in these experiments work based on the same principles, with the differences being the energy of the outgoing electrons and the focus of the beam. Simple schematics of an electron cannon and electron gun are depicted in Figure 2.3. The electron gun uses focusing optics to achieve a narrow beam of electrons that can be focused over 30 cm away. Precise aiming and alignment are required to intersect the gas expansion 3-5 mm downstream from the nozzle to sufficiently ionize the expansion. The electron cannon requires little precision and has fewer adjustable parameters since it simply sprays a diffuse wash of electrons over the entire supersonic expansion.

The east instrument used a home-built electron gun placed in location (a) in Figure 2.1, while the west instrument used a commercial gun placed in location (b) with very different specifications but based on the same principles. The home-built gun will be described first. Electrons are produced by running a current over a thoria coated iridium filament. The electrons that are emitted from the tip of the filament are pushed away by a cathode cup with a negative potential of −50 V to −200 V relative to the filament. Both the filament and the cathode cup are floated at roughly −1 kV relative to ground. The electron output is most closely tied to temperature of the filament and the electric field nearby, but those are not easily measured. The filament current is adjusted as the filament heats up and eventually held constant at ~10A for a 0.050” wide filament or 5-7A for a 0.028” filament. Higher cathode voltages made the electron output significantly more sensitive to changes in

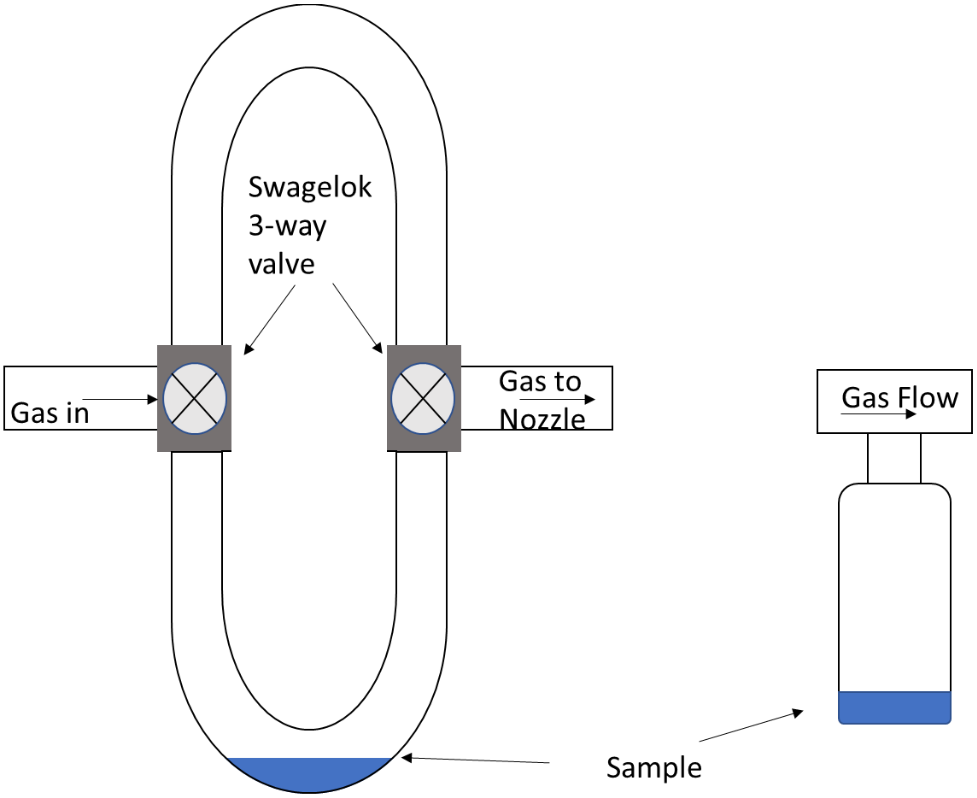

Figure 2.2 Schematic diagram of the two sample holders used in these experiments. See text for details.

filament current. Electrons then pass through three electrodes that make up the einzel lens. The first and last electrodes have a 1 mm diameter grounded aperture, while the middle plate holds an adjustable potential typically between −500 V and −1300 V. After exiting the einzel lens, the electrons are aimed by two sets of deflectors, first vertical then horizontal to direct the beam to the region directly in front of the nozzle. Each of the deflector plates are attached to Agilent E3612A power supplies which provide an adjustable 0-135 V. The electron gun is placed opposite the nozzle, so the gas expansion and electron beam are facing each other as depicted in Figure 2.3

The commercial electron gun (Southwest Vacuum Devices, Inc., CE 3K/5U) used in the west instrument has all the same components, but with a few key differences. The filament is a simple 0.02" diameter tungsten wire. It is placed under the hole of an anode cup. The potential of this cup is set to be between +20 V and 100 V relative to the filament, which pulls the electrons away from the filament after they are emitted. While these electron guns worked well, they are no longer in production. After all the remaining filaments had burnt out the electron guns had to be disassembled for replacement. The filament is attached to an emitter-post assembly which consists of a ceramic disk and two isolated metal leads through it. The tungsten wire is bent in a triangular shape with 0.008-0.011" between the highest point of the filament and the anode cup. The output of electrons is extremely sensitive to the exact placement of the filament, but the brittleness of the tungsten wire, particularly after spot welding, made adjustments nearly impossible. Additionally, each filament only lasted for a few weeks in contrast to the 4-6 months of the commercially made electron guns. It was eventually concluded that repairing the electron guns from Southwest Vacuum Devices was not viable.

The electron cannon was initially designed as the filament and cathode cup portion of a new custom electron gun. The original design had a MACOR plate with throughput posts to electrically isolate the filament from the cathode cup as shown in Figure 2.3. The filament was a 0.028" wide thoria coated iridium ribbon. The cannon had no means of aiming outgoing electrons, so it was placed 2-3 cm withdrawn from the nozzle and 5-10 mm downstream. This allowed the electrons to intersect with the entire supersonic expansion of the gas sample. Both the filament and the cathode cup are floated at between −100 V to −300 V relative to ground. Compared to the electron guns this voltage is significantly lower thus giving off lower energy electrons. The metal cup surrounding the filament has been used as both a cathode cup with a negative voltage and the filament slightly above the cup as shown in Figure 2.3, and as an anode cup with the filament below the hole each with roughly equal success. Typical current over the filament ranges from 5 A – 8 A.

There are several drawbacks and concerns with using the electron cannon long-term. Because the electrons from the cannon are not focused, they are not all collected into the faraday cup and this causes the nozzle to heat up considerably. The Teflon tubing that leads to the nozzle melted and had to be replace with stainless steel because of melting. In one instance the current over the filament was increased to over 11 A which caused the MACOR base to crack. This extreme heat must be considered when designing experiments with the electron cannon and excited anion states creating hotbands are a significant possibility.

A few adjustments were made to try to decrease the heat produced: first the MACOR base was replaced with copper to increase heat dissipation; second, the anode cup was removed leaving a bare filament to produce electrons; third, a grounded metal plate was placed between the filament and the nozzle to reduce the electron flux on the nozzle. All these things were done without any loss of ion signal for the test species of O^-, NO^-, and O_2^-. Filament lifetime is another concern, as an electron gun can have lifetimes of 6-12 months the electron cannon filaments typically last 2-4 months. This is likely also due to the extreme temperature.

2.3 Time-of-Flight Mass Spectrometer

The anion packet expands into a region between two metal plates, an extraction plate and the grounding electrode of the acceleration stack. About 2 ms after the nozzle fires, an adjustable voltage (Directed Energy Inc., PVM-4210 pulse generator) is applied to the extraction plate to repel the anions down a Wiley-McLaren[39] time-of-flight mass spectrometer.[46] The anions travel through 10 circular electrodes with increasing voltage from 0 V to +2.5 kV. Two sets of deflectors (supplied by two Agilent E3612A power supplies) are used to steer the beam. The anions then enter a decelerating einzel lens consisting of three electrodes, the first and last held at the +2.5 kV float voltage and the center electrode at a relative −800 V to −1200 V which focus the beam. After leaving the einzel lens the anion beam is referenced to ground in a stainless-steel tube called the potential switch. When the extraction plate fires, the potential switch is floated to +2.5 kV by a DEI PVX-4140 high voltage pulser (~15 ns rise time). After an adjustable delay of 6-30 μs the tube is returned to ground, which references the ions inside to ground. We control which ions are allowed to travel into the field-free region of the tube by adjusting the time delay such that only some ions are in the potential switch when it is grounded.

The ions are detected at the end of the TOF-MS by an in-line 25 mm diameter chevron-configured dual microchannel plate (MCP) detector[37,40] (Burle, Inc.). The TOF tube is shielded from the electric field of the MCP detector by a grounded 70 wires-per-inch mesh (Precision Eforming, LLC) with 90% maximum transmission a few mm in front of the detector. The MCP signal is amplified (Phillips Scientific, model 6931, DC-100 MHz) and output to a digitizing oscilloscope (Tektronix Inc., model TDS3032).

The ion spectrum can be converted from time-of-flight to mass-to-charge by using equation 2.3.1 as follows:

$$t = a\sqrt{\frac{m}{z}} + t_0, \tag{2.3.1}$$

where t is time, m/z is the ratio of mass to charge, a and t_0 are calibration constants based on the specifics of this instrument. By measuring the time-of-flight of two known mass peaks a and t_0 can be determined as follows:

$$a = \frac{t_1 - t_2}{\sqrt{m_1} - \sqrt{m_2}} \tag{2.3.2}$$

$$t_0 = \frac{t_1\sqrt{m_1} - t_2\sqrt{m_2}}{\sqrt{m_1} - \sqrt{m_2}} \tag{2.3.3}$$

Once calibrated any other peak can be identified by mass and the laser can be timed to intersect with the ion of interest to eject an electron into the velocity map imaging assembly.

2.4 Photoelectron Velocity Map Imaging Assembly

The VMI lens[18,19,47] is a series of four circular copper electrodes which sit perpendicular to the ion beam. The top three plates are 4” in diameter, are placed 1” apart and have a 1” diameter opening in the center. The fourth plate was added for the possibility of imaging photofragments but is not in use and is grounded. The ions enter between the second and third plates from the top and upon photodetachment the electrons are projected upward by the focusing electrodes. The electrode below the ion beam is held at 100–400 V negative potential (Hewlett-Packard, 6516A power supply), the middle plate is grounded, and the top plate is held at 200–800 V. This focusing allows each electron to be mapped onto the detector based solely on its velocity vector, independent of the location of photoionization within the VMI.

The ratio of the top and bottom electrodes is optimized to best focus the electrons onto the detector and is held constant at 1.98-2.02. The magnitude of the voltages determines the size of the electron packet when it reaches the detector. Lower voltages give higher resolution, but lower efficiency. The entire VMI lens is surrounded by a µ-metal shield which blocks external magnetic fields from affecting the electron trajectory. An electroformed nickel mesh (333 wires per inch, Precision Eforming, LLC., 70% maximum transmission) is placed ~0.65" prior to the detector in order to screen the photoelectrons from the detector voltages.

The electrons are detected by a 40 mm position sensitive dual-chevron MCP detector coupled to a P43 phosphor screen. The front surface of the first MCP is held at +2.00 kV while the exit of the second MCP is at +3 kV. An additional +1 kV potential (Directed Energy Inc., PVM-4150) is supplied at the exit for a 100-200 ns time window after the laser fires. This increased potential amplifies the detector signal when we expect photoelectrons to arrive. The phosphor screen is held at +6.5 kV (Burle PF 1054 power supply) The electron signal is multiplied by the MCP detector which then strikes the phosphor screen, generating photons. The light from the photons is coupled to an external window by a fiber optic bundle where it is imaged by a thermoelectrically cooled Photometrics CoolSnap MYO with 2.8 Megapixels (1940×1460) resolution. The *Cool Image* data acquisition software is used to record the image.

2.5 Laser systems

Two laser systems were used to perform the experiments in this work: an Nd:YAG nanosecond laser system (Spectra Physics Inc., Quanta-Ray Lab 130-50) and a tunable nanosecond dye laser (Continuum DCP 6100).

The fundamental of the Nd:YAG is 1064 nm and has a maximum energy per pulse of 320 mJ/pulse. This output may be frequency doubled by a Type II potassium dideuterium phosphate (KDP) crystal generating the second harmonic (532 nm) with a maximum of 70 mJ/pulse. The third harmonic can be generated by frequency mixing with the residuals of the fundamental to produce pulses at 355 nm with a maximum of 30 mJ/pulse. Alternatively, the second harmonic can be put through another KDP crystal to access the fourth harmonic at 266 nm and a maximum of 15 mJ/pulse. Each laser pulse has a width of ~8 ns and a 50 Hz repetition rate.

The dye laser system consists of a dye oscillator and two dye amplifiers pumped by a Continuum Surelite II-20 Nd:YAG laser. The pump laser is Q-switched at 20 Hz and the pulse width is ~ 5 ns. A motorized diffraction grating is angled to select a single wavelength from the broad-spectrum dye fluorescence. The power of the output depends heavily upon the conversion efficiency of the dye used and how close the diffraction-grating selected wavelength is to the peak fluorescence of the dye. In the current work three dyes were used. Two Rhodamine dyes, 640 and 610, have a peak fluorescence at 612 nm and 590 nm respectively and both output a maximum of 40 mJ/pulse. LDS 821 has a peak fluorescence at 812 nm with a maximum of 40 mJ/pulse. Each of these laser pulses can be frequency doubled with the proper doubling crystal. Rhodamine 640, 610 and LDS 821 output at 306 nm (6 mJ/pulse), 295 nm (6 mJ/pulse) and 406 nm (2 mJ/pulse) respectively.

The laser timing is controlled by the Stanford delay generator. The delay between the flash lamp trigger and the Q-switch is controlled to tune the power output with the maximum power achieved at 180 µs. The Q-switch timing is scanned to coincide with the arrival of the ion of interest to photodetach electrons. There are two primary ways of determining a good temporal overlap: signal from the neutral molecules or fragments, or signal from the photoelectrons. A 4 kV potential can be applied to the reflectron to deflect ions while allowing neutral molecules to pass. If the initial ion signal is strong enough then a scan of the Q-switch timing will reveal a signal in the in-line MCP detector when the ions and laser pulse overlap in time. If no neutral signal can be observed, then the overlap can be optimized by maximizing the photoelectron signal in real time.

2.6 Reflectron time-of-flight mass spectrometer

In addition to the VMI assembly for photoelectron spectroscopy, the west instrument is equipped with a single-stage linear-field reflectron mass spectrometer that is used to obtain photofragment-ion mass-spectra.[38] The reflectron assembly is a grounded stainless-steel electrode (4.173” OD, 1/32” thick) with a 0.315” diameter aperture, followed by 26 stainless steel circular electrodes (3.15” OD, 1/32” thick) series of electrodes with a 2.025” diameter opening. The plates are angled in such a way as to deflect ions into an off-line MCP detector which is below the incoming ion beam path slightly before the VMI assembly. The final plate is attached to a high-voltage power supply (Bertan, 205A-05R), which defines the reflectron voltage, Vf and all subsequent plates are connected to the next by 1.0 MΩ high precision resistors until the grounded plate.

Photofragments are detected by an off-axis dual checron MCP detector (Burle, Inc.). A wire grid biased to + 20 V covers the detector to repel low energy electrons. The signal from this detector is amplified and sent to the oscilloscope just like the in-line MPC detector signal. It is important to collect signal in the off-line MCP detector with the laser off as well to determine that the detected fragment originates from the ion-laser interaction.

The time it takes for an ion to reach the off-axis detector depends upon its mass and the reflectron voltage. A more massive particle penetrates more deeply into the reflectron field before being deflected. To determine the mass of the photofragment, first the parent ion is focused onto the the off-axis detector by adjusting the reflectron voltage V_p and the time of arrival is recorded. Fragment ions are then focused onto the same detector such that the arrival time is the same as the parent ions, by using a lower V_f. Since the time-of-flight has been set equal the following ratio gives the relationship between the parent and fragment ion masses:

$$V_f = V_P \frac{m_f}{m_p} \tag{2.6.1}$$

If there are only a few fragment ions, then the mass spectrum can be recorded by scanning the reflection voltage to set the TOF of each fragment equal to the TOF of the parent ion. If there are many fragments, such as for large clusters, then after two fragments have been identified a calibration can be performed in the same way as in section 2.3 for the in-line detector to obtain a full photofragment mass spectrum.

2.7 Photoelectron Data Collection and Analysis

Photoelectron signal from the CCD camera is collected and summed in the Cool Image program[48]. Images were accumulated for ~10^6 experimental cycles. Background images were obtained by turning off the ion extraction plate, so the laser sampled the detection region while the ion of interest was not present. Background images were also summed and subtracted from photoelectron images.

The image recorded by the CCD camera is a two-dimensional projection of the three-dimensional photodetached electron wave. The BAsis Set EXpansion[49] (BASEX) program reconstructs the three-dimensional distribution and outputs a slice through the center by means of an inverse Abel transformation.[50] This distribution is given in two forms: a radial distribution and polar distribution. The radial distribution is created by integrating the image over all angles. The well-known photodetachment transition from atomic O^- is used to calibrate the radial spectrum to convert from radius (which is proportional to velocity) to energy.

The photoelectron angular distribution (PAD) is obtained by integrating over a specific radial width using MATLAB code written by the author, which is included in full, with notes on typical use in appendix A. In brief, the radial distribution is plotted, and the user is asked how many peaks to analyze and to specify their radii. Not using a traditional peak-finder allows for non-traditional peaks with low prominence or even slices of a single peak to be analyzed. The photoelectron intensity is summed over the specified radii creating the PAD, $I(\theta)$. For each peak, the anisotropy parameter β is obtained by a least-squares fit to the formula (1.2), which gives the PAD in terms of the angle θ within a second-order Legendre polynomial and a single parameter β.

2.8 Instrumental Repairs and Improvements

The purpose of this subsection is to outline a few important repairs that have been performed or may need to be performed soon and to provide written documentation to future users of the west instrument.

2.8.1 Resolution loss and Offline Detector Access

Early in 2019 a significant decrease in energy resolution of photoelectrons was discovered in comparing O^- calibrations from 2017. The FWHM of earlier measurements of the O^- electron affinity peak was a factor of 2.5 more narrow. It is likely the cause of this resolution loss is due to either the pulsed nozzle or the electron cannon configuration. Attempts at solving this with electronics settings, focusing of the ion optics or adjusting the timing or position of the laser to achieve better overlap with the ion packet were unsuccessful. Additionally, the focusing of the VMI by checking the spacing between plates and varying voltages made no measurable improvement.

A significant increase in resolution was achieved by tightening the aperture for the ion beam entering the VMI stack. The previous aperture, which was a hole in the μ-metal shield of ~3 mm, was covered by a copper plate with a ~1.5 mm hole. This copper plate also covers the hole that photofragment ions pass through *en route* to the off-line detector, which makes fragmentation experiments currently unavailable. The proper solution to this is to order a new custom μ-metal shield with a smaller hole. The resolution issue should be revisited once an electron gun can be machined to replace the electron cannon.

2.8.2 Turbo Pumps

High pressure in the detection region ($>10^{-8}$ Torr) can cause excessive background signal when imaging with UV wavelengths. For a time, pressures of 10^{-7} Torr were the best achievable in the detection region. We discovered that the turbo pump attached to the detection region had its fan blades coated in oil droplets. To properly address this the fan blades must be disassembled and cleaned individually and then remounted and balanced so that high speeds can be achieved without damaging the pump. This will likely require assistance from the manufacturer. This pump was not repaired, but rather swapped with the turbo pump most downstream in the TOF region where the pressure requirements are lower. It is likely that oil was pulled from the backing pump either due to improper venting or over years of use. If this occurs again both pumps should be sent to Leybold, Inc. for repairs.

2.8.3 10” Diffusion Pump

During the summer months high humidity causes water to condense on the chilling lines of the diffusion pump (DP). After many years of use, this degraded the wire connections to the heating elements which eventually caused rusting and cracking. The heating elements of the diffusion pump are intact, but the threaded connections are heavily damaged, and a custom connection had to be machined for one of them. If the connections degrade any more the entire heating elements will need to be replaced. The first noticeable sign of this will likely be an increase of the time it takes for the DP to heat to an operational temperature from around 20 minutes to an hour or more. The wires use should be no smaller than 10 gauge because of the high heat from the DP and the high current.

CHAPTER 3: LOCAL ELECTRON DENSITIES IN MODELING OF PHOTOELECTRON ANGULAR DISTRIBUTIONS

In Chapter 1, we discussed the modeling of photoelectron angular distributions[51,52] (PADs) for atomic anions using the Cooper-Zare central-potential formula[26,27] and the s-p mixing model for molecular anions. In this Chapter, we will explore some of the applications of the s-p mixing model[22] and their required assumptions, first by summarizing the details of the model[36] and then by using computational results to refine the application of the model to physical systems.

3.1 Introduction

Consider one-photon photodetachment within a single-electron approximation. Assume that the initial state of the electron is represented by a linear combination of one *s* and one p type functions placed at the same center in the molecule.[22] The corresponding model function for the initial state is given by

$$|\,\psi_{sp}\rangle = \sqrt{1-\gamma_p}|s\rangle + \sqrt{\gamma_p}|p\rangle, \tag{3.1}$$

where γ_p is the fractional p character of the state, with $0 \leq \gamma_p \leq 1$. A photon carries one unit of orbital angular momentum, resulting in the of $\Delta l = \pm 1$ selection rule, where *l* is the orbital angular momentum. Upon photodetachment from the initial state described by Eq. 3.1, the outgoing electron will be generally represented as a superposition of s, p, and d partial, emitted via the electric-dipole allowed transitions $s \rightarrow p$ and $p \rightarrow s, d$. The intensities (cross-sections) of these waves will be dependent on electron kinetic energy (eKE $\equiv \varepsilon$). According to the Wigner-law,[28] in the near-threshold regime, $\sigma_l \propto \varepsilon^{l+1/2}$. The anisotropy of the PAD for detachment from this mixed s-p orbital can be described by the following equations as explained in Section 1.3[22,26,27]:

$$\mathrm{I}(\theta) = \frac{\sigma}{4\pi}[1 + \beta \mathrm{P}_2(\cos\theta)] \tag{3.2}$$

$$\beta_{sp}(\varepsilon) = \frac{2(1-\gamma_\mathrm{p})\mathrm{B}_1\varepsilon + 2\gamma_\mathrm{p}\mathrm{A}_1^2\varepsilon^2 - 4\gamma_\mathrm{p}\mathrm{A}_1\varepsilon\cos(\delta_2-\delta_0)}{\gamma_\mathrm{p} + 2\gamma_\mathrm{p}\mathrm{A}_1^2\varepsilon^2 + (1-\gamma_\mathrm{p})\mathrm{B}_1\varepsilon}. \tag{3.3}$$

Equation 3.3 includes 4 parameters, A_1, B_1, γ_p, and the phase shift $\cos(\delta_2 - \delta_0)$, which can all give physical insight into applications of this model. A_1 and B_1 are model proportionality parameters that arise from the application of the Wigner-law[14]:

$$\frac{\sigma_2}{\sigma_0} = \frac{\chi_{1,2}^2}{\chi_{1,0}^2} = \mathrm{A}_1^2\varepsilon^2 \tag{3.4}$$

$$\frac{\sigma_2}{\sigma_0} = \frac{\chi_{0,1}^2}{\chi_{1,0}^2} = \mathrm{B}_1\varepsilon. \tag{3.5}$$

Physically, the A_1 parameter describes the relative scaling of the $p \rightarrow d$ and $p \rightarrow s$ channels and B_1 describes the relative scaling of the outgoing $s \rightarrow p$ and $p \rightarrow s$ channels.

We can rearrange Equation 3.3 to give:

$$\beta_{sp}(\varepsilon) = \frac{2\left(\frac{1-\gamma_\mathrm{p}}{\gamma_\mathrm{p}}\right)\frac{\mathrm{B}_1}{\mathrm{A}_1}\varepsilon + 2\mathrm{A}_1\varepsilon^2 - 4\varepsilon\cos(\delta_2-\delta_0)}{\frac{1}{\mathrm{A}_1} + 2\mathrm{A}_1\varepsilon^2 + \left(\frac{1-\gamma_\mathrm{p}}{\gamma_\mathrm{p}}\right)\frac{\mathrm{B}_1}{\mathrm{A}_1}\varepsilon}$$

$$= \frac{2\mathrm{Z}\varepsilon + 2\mathrm{A}_1\varepsilon^2 - 4\varepsilon\cos(\delta_2-\delta_0)}{\frac{1}{\mathrm{A}_1} + 2\mathrm{A}_1\varepsilon^2 + \mathrm{Z}\varepsilon}, \tag{3.6}$$

which, aside from the phase shift, allows us to reduce the number of parameters to two: A_1 and $\left(\frac{1-\gamma_\mathrm{p}}{\gamma_\mathrm{p}}\right)\frac{\mathrm{B}_1}{\mathrm{A}_1} \equiv Z$. The phase shift arises due to interactions of the outgoing electron waves with the remaining neutral core. These interactions are largely negligible and can be approximated well with $\cos(\delta_2 - \delta_0) \approx .95$. [22,33] For a given A_1, Z describes the relative scaling of the outgoing $p \rightarrow s$ and $s \rightarrow p$ channels (B_1) weighted by the relative contributions of *s* and p components of the initial state $\left(\frac{1-\gamma_\mathrm{p}}{\gamma_\mathrm{p}}\right)$. Z ranges from Z = 0, for a pure p state to $Z \rightarrow \infty$ for a pure *s* state.

Applications of this model require intuition of appropriate values of A_1 and Z to have predictive power. To gain this insight we examine the radial dipole integrals that define A_1 and B_1 according to Equations 3.4 and 3.5. If we assume that the bound orbitals and the free electron waves are defined by their radial functions $R_{n,l}(r)$ and $R_{free,l\pm1}(r)$, respectively, multiplied by the corresponding spherical harmonics, then the radial dipole integrals are given by:

$$\chi_{l,l\pm1} \equiv \langle R_{free,l\pm1} \mid r \mid R_{n,l}\rangle. \tag{3.7}$$

If we assume no interaction of the electron with the remaining neutral, the radial functions of the free electron waves $R_{free,l}$ can be represented by spherical Bessel functions,[53,54] $j_l(kr)$. Explicitly writing A_1 and B_1 in terms of these integrals gives:

$$\mathrm{A}_1\varepsilon = \frac{\chi_{1,2}}{\chi_{1,0}} = \frac{\int_0^\infty j_2(kr)r^3 R_{np}(r)dr}{\int_0^\infty j_0(kr)r^3 R_{np}(r)dr} \tag{3.8}$$

$$\mathrm{B}_1\varepsilon = \frac{\chi_{0,1}}{\chi_{1,0}} = \frac{(\int_0^\infty j_1(kr)r^3 R_{n's}(r)dr)^2}{(\int_0^\infty j_0(kr)r^3 R_{np}(r)dr)^2} \tag{3.9}$$

where the prime in $R_{n'p}$ denotes that *s* and p initial states do not have to correspond to the same principle quantum number.[33]

To simplify this further, we apply a Wigner-like slow-electron limit[28,55,56] as was assumed by Hanstorp *et al.*[14] in their definition of A_1 in Equation 3.4. In the region of significant overlap between the free-electron waves and the initial bound state, this limit is defined as $kr \ll 1$. In this limit, we can express the spherical Bessel functions as the first term of their Maclaurin series expansion:

$$j_l(kr) = \frac{2^l l!}{(2l+1)!}(kr)^l, \ \text{for } kr \to 0. \tag{3.10}$$

Substituting this expression into Equations 3.8 and 3.9 gives us:

$$\mathrm{A}_1 = \frac{2}{15}\frac{\int_0^\infty r^5 R_{np}(r)dr}{\int_0^\infty r^3 R_{np}(r)dr} \tag{3.11}$$

$$\mathrm{B}_1 = \frac{2}{9}\frac{(\int_0^\infty r^4 R_{n\prime s}(r)dr)^2}{(\int_0^\infty r^3 R_{np}(r)dr)^2}, \tag{3.12}$$

and additionally, the ratio of $\mathrm{B}_1/\mathrm{A}_1$ used in the definition of Z for Equation 3.6:

$$\frac{\mathrm{B}_1}{\mathrm{A}_1} = \frac{5}{3}\frac{(\int_0^\infty r^4 R_{n\prime s}(r)dr)^2}{\int_0^\infty r^3 R_{np}(r)dr \int_0^\infty r^5 R_{np}(r)dr}. \tag{3.13}$$

Note that in the low energy regime both A_1 and B_1 are independent of *k* and, therefore, ε. Additionally, the high powers of *r* under the integrals imply a strong dependence of the coefficients and their ratio on the long-range parts of the radial functions, i.e. the diffuse tails[57] of the parent anion orbital. Any wavefunction density at large distances from the center will significantly contribute to formulation of these parameters.

If the *s* and *p* components of the detachment orbitals are assumed to be hydrogenic then the integrals in the previous equations are analytically solvable. Substituting in the hydrogenic radial functions for the 2*s*-2*p* case with the effective charges ξ_{2s} and ξ_{2p} respectively we get[36]

$$\mathrm{A}_1 = \frac{16}{\xi_{2p}^2}\ \text{Hartrees}^{-1} \tag{3.14}$$

$$\frac{\mathrm{B}_1}{\mathrm{A}_1} = \frac{8}{3}\left(\frac{\xi_{2p}}{\xi_{2s}}\right)^7. \tag{3.15}$$

Note that in general ξ_{2s} and ξ_{2p} are not the usual effective nuclear charges predicted by Slater's rules,[58] but rather the effective charges experienced by the long-range parts of diffuse anion orbitals accounting for the screening of the inner electrons.

Again, note the high-power dependence of B_1/A_1 on ξ_{2p}/ξ_{2s}. Previously, we noted the high-power dependence of A_1 and B_1, which means that the effective charges in this case describe the behavior of these diffuse tails. The 2*s* and $2p$ tails both interact with a similarly charged nearly neutral core. This allows us to reasonably assume $\xi_{2p} = \xi_{2s}$, which means $\frac{B_1}{A_1} = \frac{8}{3}$.[36]

With specific values of A_1 and Z the β(ε) trends for PADs from s-p mixed orbitals can be modeled. The evaluation of A_1 for the atomic cases of $O^-$and C^- have been preformed by empirical fitting of experimental data to the Hanstorp[14] approximated Cooper-Zare formula[26,27] given in Equation 1.5, which gives $A_1(O^-) = 0.55 \pm .045\ \mathrm{eV}^{-1}$ [59-62] and $A_1(C^-) \approx 0.75\ \mathrm{eV}^{-1}$.[61,63] As we move from atomic to molecular anions, it must be noted that the s-p model involves the so-called central-atom approximation, which assumes that both the *s* and *p* contributions to the s-p mixed orbital are located on a single center in the molecular frame. Note that the central-atom approximation would be more appropriately called the central-point approximation, because the "atom" in it does not have to be a real atom. It can be a pseudo-atom, i.e. merely an expansion center chosen within the molecular frame, not necessarily coinciding with any of the physical atoms comprising the molecule. For example, within this approximation, the π_g^* HOMO of O_2^- is described as a predominantly *d* function placed at the center of the O–O bond.

However, in the cases of (nominally) sp^2 hybrid orbitals of cyclic organics, the expansion center is often chosen to coincide with the target (deprotonated) carbon.

Historically, A_1 for such a molecule has been assumed to be equal to A_1 for the atom on which most of the electron density is localized.[34,35] This method has worked exceptionally well for some molecules e.g., pyridinide anion,[34] but less so for others-e.g., furanide[64] and oxazolide[65] anions.

3.2 Local Charge Density

The highest occupied molecular orbital (HOMO) of a molecular anion is often localized predominantly on a single atom within the molecule. This is especially true for many deprotonated organic molecules, where the HOMO character reflects the hybridization state of the deprotonated atom. The valence orbitals of anions are inherently more diffuse than those of the corresponding neutrals because the core is shielded by the other electrons, lowering the effective nuclear charge. A well-defined atomic charge within an anionic molecule could be used to quantify the spatial extent of the electron.

Mulliken population analysis[66] is a model that attempts to define atomic charges based on the density matrix from geometry optimizations. However, this analysis is strongly dependent on the choice of basis set. Wiberg, *et al.*[67] analyzed several methods of obtaining insightful atomic charges and concluded that Hirshfeld[68] charges provide linear relationships with parameters such as hybridization and carbon acidity which correlate with atomic charge and is the method of choice. Hirshfeld charges are additionally nearly independent of the choice of basis set.

Computations were performed on several deprotonated heterocyclic aromatic molecules using the Q-chem[69] software package to optimize their geometry at the B3LYP level of theory with the aug-cc-pVDZ and aug-cc-pVTZ basis set. The Mulliken and Hirshfeld[68] population analyses were used to calculate the effective local charge on the deprotonated carbon atom. These values are found in Table 3.1. Mulliken population analysis does not provide basis-set independent insight into a physical property of the anion. The Hirshfeld population analysis, however, preserves trends across basis sets and can help describe the local electron density around the deprotonation center.

These deprotonation centers act as the central atom for the s-p hybrid orbital for the anions. The greater the magnitude of the negative charge localized on the center, the greater the screening of the valence electrons, which is, in turn, described by a smaller effective nuclear charge experienced by the long-range tails of the valence orbitals. According to Equation 3.14, the parameter A_1 is inversely proportional to the square of the effective nuclear charge ξ_{2p} defining the radial dependence of the p component of the s-p model function in Equation 3.1.[36] Because of this inverse-square dependence on the effective nuclear charge, A_1 is particularly sensitive to variations in ξ_{2p} and, therefore, the local charge localized on the central atom. This property makes an accurate evaluation of the local charges within the molecular system extremely important for its model description. It is therefore clear that one cannot use Mulliken charges for this purpose, if only because of their strong (and unphysical) dependence on the basis set used in the calculation. Hirshfeld charges, on the other hand, are largely basis-set independent and have been shown to provide an accurate description of the local molecular environment. Therefore, Hirshfeld rather than Mulliken charges will be used in our modeling.

This discussion also gives the insight that all other things being equal, a larger-magnitude local/Hirshfeld charge would lead to a less tightly bound electron and thus a smaller detachment energy. While there is not a quantitative relationship between

Table 3.1 Hirshfeld and Mulliken charges on the deprotonated carbon calculated with the aug-cc-pVDZ and aug-cc-pVTZ basis sets.

Molecule	Hirshfeld pVTZ	Hirshfeld pVDZ	Mulliken pVTZ	Mulliken pVDZ
Isoxazolide	-0.340053	-0.338796	-0.698287	-0.457789
Thiophenide	-0.361037	-0.357995	-0.703212	-0.985494
Furanide	-0.386076	-0.383001	-0.592924	-0.486369
Thiazolide	-0.236191	-0.235525	-0.778838	-0.534907
Oxazolide	-0.314710	-0.311225	-0.554975	-0.321424

Hirshfeld[68] charge and effective nuclear charge, this gives a qualitative connection between *ab initio* computations and PAD parameter A_1, which was previously only obtainable for atomic anions.

3.3 Trends in Heterocyclic Aromatics

The s-p mixing model was applied to five different deprotonated heterocyclic aromatics. Plots of the anisotropy parameter versus eKE are given in Figure 3.2. The initial analysis (shown by the red line) fit the data using the s-p model function Equation 3.6 with $\frac{B_1}{A_1} = \frac{8}{3}$, $\cos(\delta_2 - \delta_0) \approx .95$ and $A_1 = 0.75\ \mathrm{eV}^{-1}$ with only γ_p as a fit parameter.[22,33,34] The above A_1 value was determined by examining photodetachment from isolated C^- anions. In each of the molecular anions discussed here, have much of the electron density of the HOMO is localized on the deprotonated carbon, which makes the above assumption for A_1 reasonably good. This is evidenced by the quality fits of these lines.

Here, we take a step further and consider that not the entire charge of the excess electron is localized on the deprotonated carbon. This is clearly borne out by both the Mulliken and Hirshfeld charges of the deprotonated centers summarized in Table 3.1, all of which are, as expected, smaller than 1 in magnitude. As a result, these anions should have more diffuse wavefunctions, leading to larger A_1 values, compared to the atomic carbon anion.

Moreover, the local charge (and the effective nuclear charge) describing the deprotonated center will be different not only compared to C^-, but also from system to system, depending on the molecular anion's chemical identity and electronic structure. The fact is also borne out by the different magnitudes of the Hirshfeld charges on the photodetachment centers calculated for the above molecular anions (summarized in Table 3.1).

With this realization in mind, each data set in Figures 3.1-3.3 was fit to Equation 3.6 with both A_1 and γ_p treated as adjustable fit parameters. The other two parameters, $\frac{\mathrm{B}_1}{\mathrm{A}_1}$ and $\cos(\delta_2 - \delta_0)$ were left the same as in the previous analysis. The phase shift is due to interactions of the outgoing electron partial waves and the neutral core is not likely to be influenced by slight changes to the effective nuclear charge. While we are allowing A_1, and thus the effective nuclear charge, to vary, remember that Equation 3.15 shows that the ratio $\frac{\mathrm{B}_1}{\mathrm{A}_1}$ is dependent on the ratio of the *s* and *p* effective nuclear charges as viewed at long range, i.e. far from the deprotonation center. While the charges themselves may vary, the ξ_{2p}/ξ_{2s} ratio is likely to remain approximately constant, because there is no physical reason for the *s* and *p* components of the model function in the long range to exhibit divergent variations with respect to the local charge on the expansion center. These fits are displayed in Figures 3.1 – 3.3

Fitting the data with an additional variable parameter obviously leads to a closer fit. However, there are physical insights gained about the electronic structure from the values of A_1 obtained from the fits and their relationship to the Hirshfeld charges. The parameters from the fits are listed in Table 3.2 and depictions of their molecular orbitals are depicted in Figure 3.4. While the deprotonated carbon carries the majority of the electron density and our model assumes detachment from a mixed s-p orbital localized on a single center, the adjacent atoms affect the local environment and hence the electronic structure of these orbitals. The local Hirshfeld charges[68] listed in Table 3.2 are defined as the sum of the Hirshfeld charges on the deprotonated carbon and the two adjacent atoms. This allows us to quantify the shielding felt by the diffuse anion orbitals.

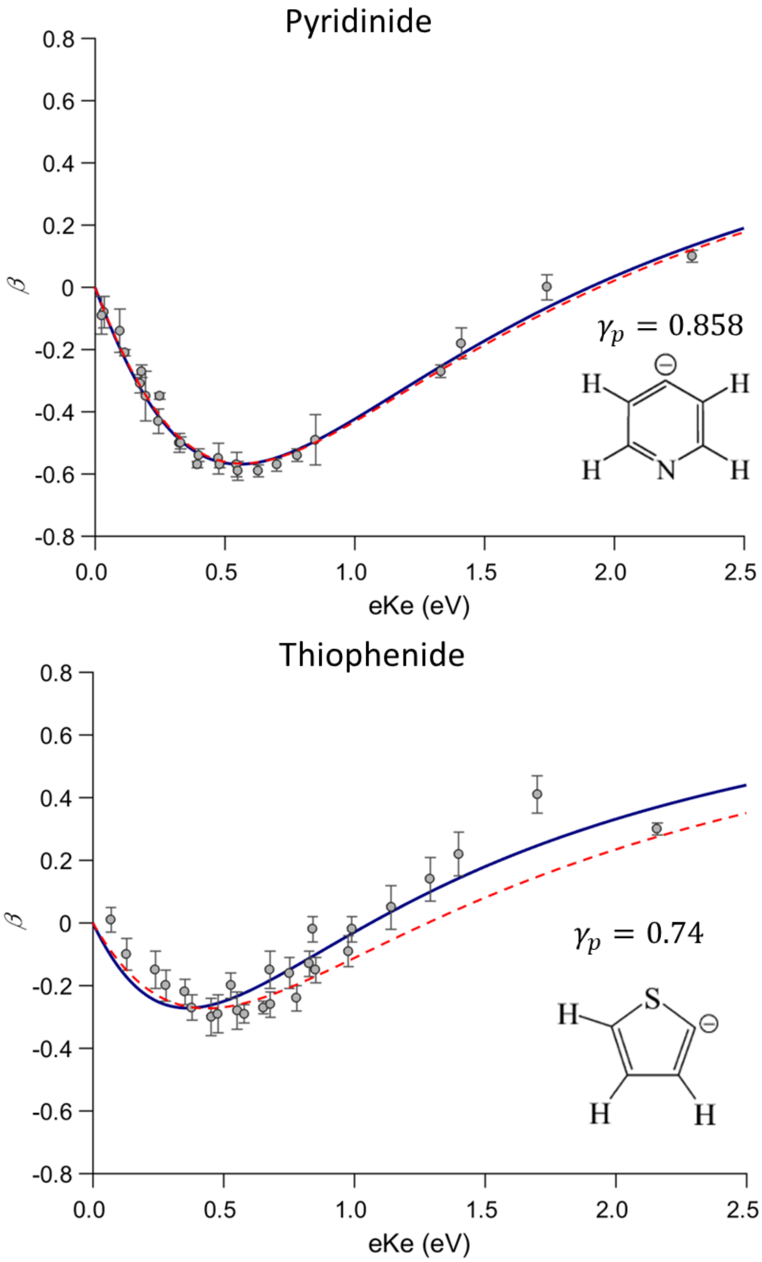

Figure 3.1 Photoelectron anisotropy parameter values for the photodetachment of pyridinide and thiophenide as functions of eKE. The dashed red curve corresponds to a fit of the s-p model with $\frac{B_1}{A_1} = \frac{8}{3}$, $\cos(\delta_2 - \delta_0) \approx .95$ and $A_1 = 0.75\ \mathrm{eV}^{-1}$ and relied on γ_p as a fit parameter. The blue line fits the s-p model with both A_1 and γ_p treated as adjustable fit parameters.

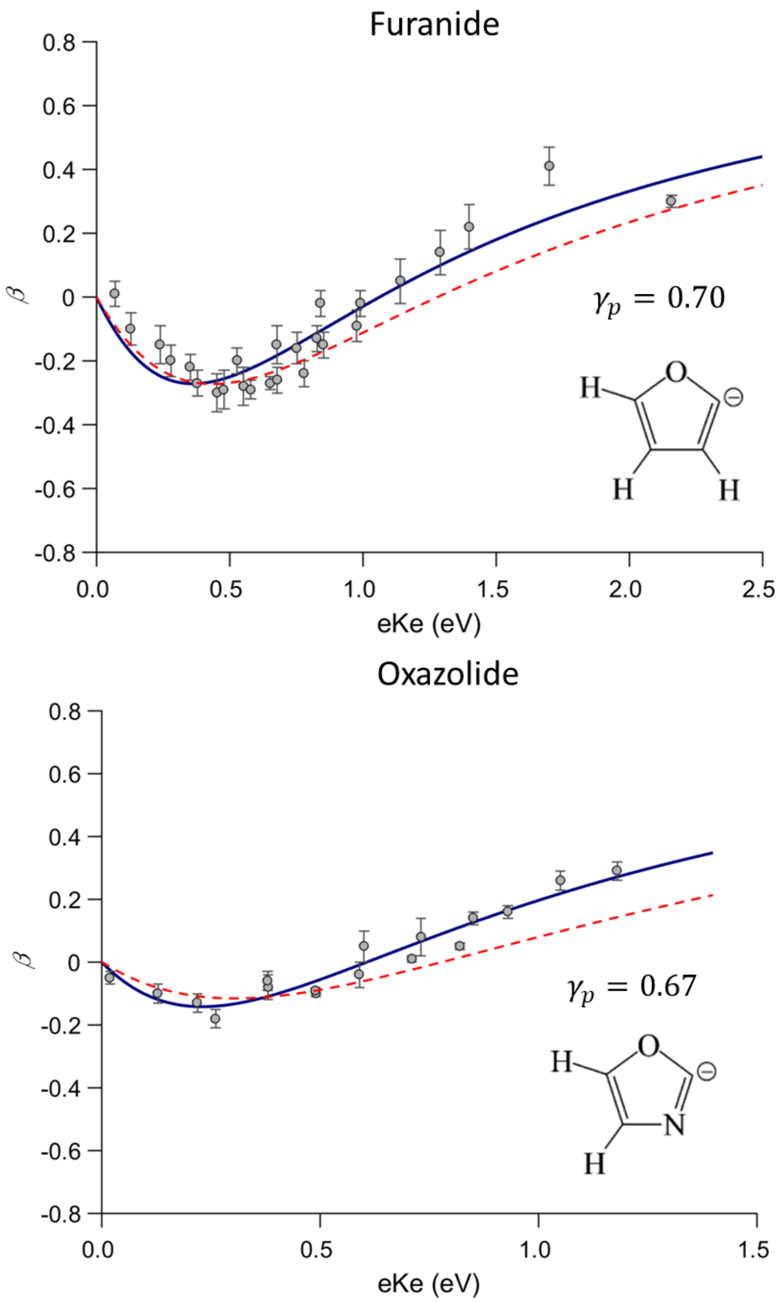

Figure 3.2 Photoelectron anisotropy parameter values for the photodetachment of furanide and oxazolide as functions of eKE. The dashed red curve corresponds to a fit of the s-p model with $\frac{\mathrm{B}_1}{\mathrm{A}_1} = \frac{8}{3}$, $\cos(\delta_2 - \delta_0) \approx .95$ and $\mathrm{A}_1 = 0.75\ \mathrm{eV}^{-1}$ and relied on γ_p as a fit parameter. The blue line fits the s-p model with both A_1 and γ_p treated as adjustable fit parameters.

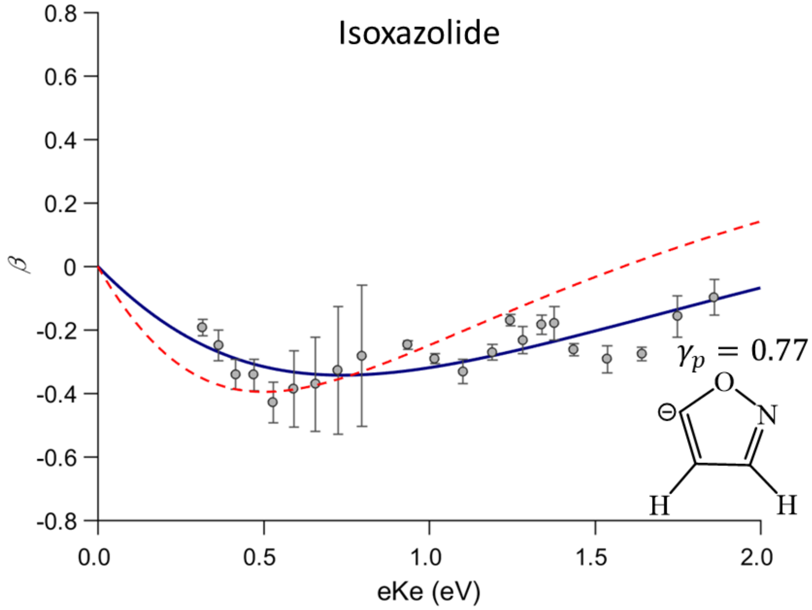

Figure 3.3 Photoelectron anisotropy parameter values for the photodetachment of isoxazolide as a function of eKE. The dashed red curve corresponds to a fit of the s-p model with $\frac{B_1}{A_1} = \frac{8}{3}$, $\cos(\delta_2 - \delta_0) \approx .95$ and $A_1 = 0.75\ \mathrm{eV}^{-1}$ and relied on γ_p as a fit parameter. The blue line fits the s-p model with both A_1 and γ_p treated as adjustable fit parameters.

Of the fits using A_1 from atomic carbon, Pyridinide was clearly the best. We attribute this observation to the local environment with the two neighboring carbon atoms largely preserving the symmetry of the deprotonated carbon, as well as not competing with it strongly for the HOMO density. Using A_1 as a fit parameter hardly changed its value. Of the molecules tested pyridinide has the lowest local Hirshfeld charge and thus the highest effective nuclear charge.

Furanide and thiophenide both have similar local chemistry near the center of the anion HOMO. The deprotonated carbon is bonded to another carbon and an oxygen or sulfur respectively both of which are electron withdrawing groups. Oxygen is more electronegative than sulfur and thus this effect is stronger in furan, resulting in a larger local Hirshfeld charge. As expected, increasing the local Hirshfeld charge leads to more electron screening and a more diffuse orbital exhibited by an increasing A_1. It is possible this effect is accentuated by a single electron withdrawing group breaking the symmetry.

In Oxazolide the electron density on the deprotonated carbon is pulled toward the electron withdrawing oxygen and nitrogen atoms. This large delocalization of electron density is evidenced by a large-magnitude local Hirshfeld charge and thus a high value of A_1 relative to atomic carbon.

At first glance isoxazolide may appear to fit the trend with low values of local Hirshfeld charge and A_1. However, there is not a clear reason why A_1 should be significantly lower for isoxazole than it is for carbon. As we will explained in Chapter 4 of this work, isoxazole likely does not always deprotonate at a single location and undergoes significant geometry changes after deprotonation. This means the data in Figure 3.3 is likely a superposition of states from multiple isomers and cannot be described by the s-p model.

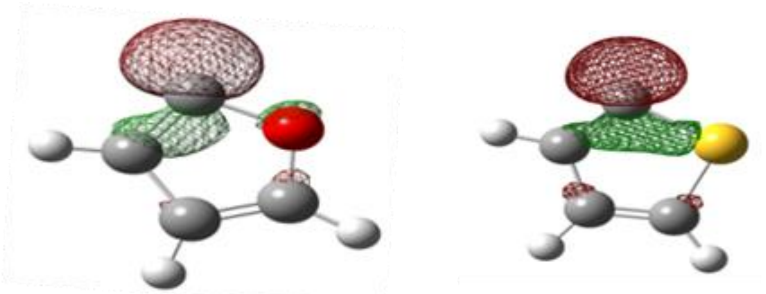

Furanide Thiophenide

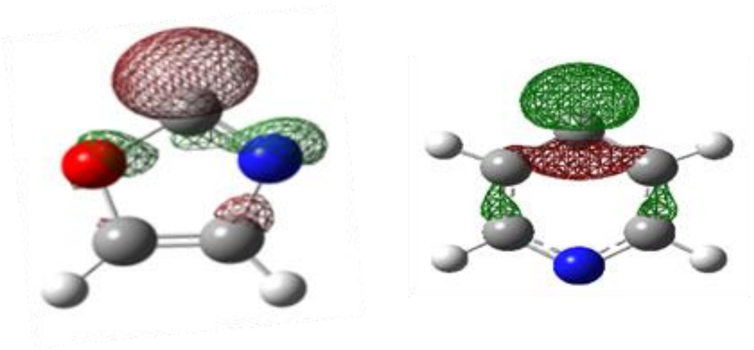

Oxazolide Pyridinide

Figure 3.4 Anion HOMOs from B3LYP/aug-cc-pVDZ calculations.[35,70] Electron density around the deprotonated carbon atom shields the diffuse anion orbitals from the largely neutral core.

For each of the molecules studied, the fractional *p*-character, γ_p, was changed by less than 2% by using A_1 as a parameter with each value well within the error bars of the original fits. This means that there is no loss of generality or added uncertainty by incorporating A_1 as a parameter in the s-p mixing model.

3.4 Conclusion

In this chapter, we have expanded upon the s-p mixing model to describe the PAD and better understand electronic structure. Allowing A_1 to be a fit parameter has given insight into trends of several physical measurements. The use of Hirshfeld charges opens up the possibility of using *ab initio* computations to predict trends in A_1 and eBE for the substitution of other heteroatoms in place of the oxygen, sulfur or nitrogen atoms in the molecules we have studied.

Molecule	Structure	Local Hirshfeld Charge*	γ_p	$A_1(eV^{-1})$
Isoxazolide	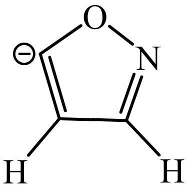	-0.702	.77(2)	.48(7)
Pyridinide	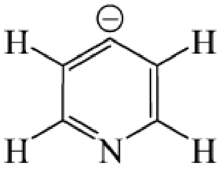	-0.661	.858(7)	.76(3)
Thiophenide	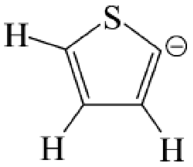	-0.751	.74(2)	.9(1)
Furanide	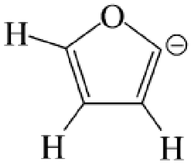	-0.769	.70(3)	1.2(2)
Oxazolide	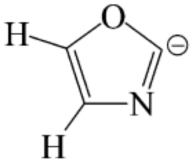	-0.815	.67(2)	1.1(2)

* The local Hirshfeld charges reported in this Table are determined by adding together the corresponding charges on the deprotonated carbon and the two neighboring atoms (with the Hydrogens included in the heavy-atom charges).

Table 3.2 Results of calculations and fitting anisotropy data to the s-p model. Local Hirshfeld charges are from B3LYP/aug-cc-pVTZ calculations. The values of A_1 and γ_p are the fit parameters in the s-p model. The value of γ_p changed less than 2% by varying A_1.

CHAPTER 4: DEPROTONATION OF ISOXAZOLE: A PHOTOELECTRON IMAGING STUDY

4.1 Introduction

Isoxazole is heterocyclic molecule, an isomer of oxazole. The oxazole and isoxazole structures are shown in the following scheme:

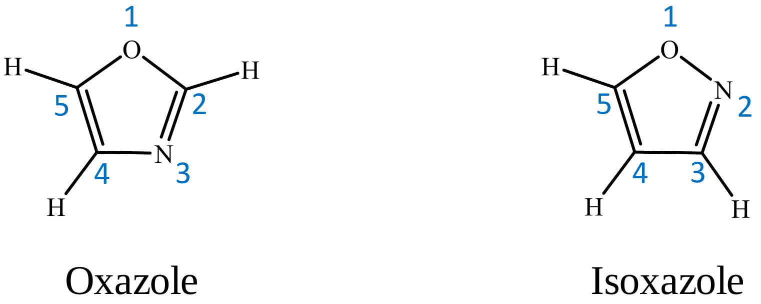

(Scheme 4.1)

The difference between the two structures is the change in location of the nitrogen atom from the third position within the heterocyclic ring in oxazole to the second position, next to the oxygen atom, in isoxazole. One of the overarching goals of this study is to investigate the chemical effect of this change.

Isoxazole, known for its straightforward synthesis, is often used as scaffolding for therapeutic agents.[9] Its other wide-ranging applications span organic synthesis, pharmaceuticals, and pesticides.[5,6] However, many important aspects of its chemistry remain unexplored, especially in regard to the radical and negative-ion derivatives. Past studies of isoxazole mostly focused on the closed-shell neutral molecule shown in Scheme 4.1 and the corresponding cation.[7,71-73] In the present work, we focus on the closed-shell anions obtained via the deprotonation of isoxazole, as well as the corresponding monovalent neutral radicals accessed in the photodetachment of the anions. These highly reactive species may play crucial roles in the variety of reaction pathways. Using a combination of experimental and theoretical techniques, we investigate their molecular and electronic structures and determine the respective anion detachment energies and neutral radical electron affinities. These properties are viewed in comparison to the analog oxazole molecule.[65]

There are three possible deprotonation sites in either oxazole or isoxazole. Following the conventional numbering system defined in Scheme 4.1, the possible deprotonation sites in oxazole are C2, C4, and C5, compared to C3, C4, and C5 in isoxazole. Each site potentially yields a distinct isomer of the respective oxazolide or isoxazolide anion. Based on the electronegativities of the neighboring atoms (increasing from C to N to O), one expects the acidity—and hence the ease of deprotonation—to decrease from C2 to C5 to C4 in oxazole and from C5 to C3 to C4 in isoxazole. These predictions are consistent with the past studies. Specifically, under the gas-phase plasma conditions similar to the experiments described here, oxazole was shown to deprotonate selectively at the most acidic C2 position,[65] while collision-induced dissociation experiments by Adams *et al.* showed preferred deprotonation of isoxazole at C5 and C3.[11] Cole *et al.* attempted to selectively deprotonate isoxazole at C5 via collisional decarboxylation of isoxazole-5-carboxylic acid, but found that upon collision isoxazole lost HCN rather than the carboxy group.[74] Computational work by Kaur *et al.* confirmed that the C5 site in isoxazole is more acidic than C4, while deprotonation at C3 led to the breaking of the O–N bond, making the C3 comparison more challenging.[75] In a study of 1H-1,2,3-triazole, a 5-member heterocyclic aromatic with three nitrogen atoms, Ichino *et al.* found that deprotonation at various carbon positions initiated fragmentation or N-N bond fission.[10]

In the present study, we explore the deprotonation of isoxazole in its gas-phase reaction with O^- radical anions and the various anion states that result. These include the C5- and C4-isoxazolide anions and the ring-open anion species resulting from isoxazole deprotonation at the C3 position. The relative energetics of the anion isomers, as well as the corresponding neutral radicals, are examined using a combination of photoelectron spectroscopy and theoretical methods.

4.2 Experimental Methods

The experiments were performed using the west negative-ion photoelectron imaging spectrometer described in detail in Chapter 2,[76] with certain changes introduced to the ion generation process, as described below. The anions were obtained by expanding a neutral isoxazole precursor seeded in O_2 or N_2O gas through a pulsed supersonic nozzle (General Valve, Inc., Series 9), operated at a repetition rate of either 20 or 50 Hz, to match that of the laser. The precursor isoxazole vapor was picked up from the liquid sample (99%; Sigma Aldrich, Inc.) kept at ambient room temperature, while the carrier gas was passed over the liquid at a backing pressure of approximately 2.5 atm. The 52 torr vapor pressure of isoxazole at 25°C resulted in a 2.5-3% mixture of the precursor and the carrier gas.

The supersonic expansion was intersected by electrons from a thoria-coated iridium filament (e-Filaments, LLC) floated at ~300V, generating negative ions via a slow secondary electron attachment mechanism. In this work, the filament was placed at various distanced downstream from the nozzle and withdrawn away from the expansion axis. A diagram of the filament locations used is given in Figure 4.1. In some of the experiments with oxygen as a carrier gas, a 5×5 cm^2 stainless steel plate, kept at the same potential as the filament, was placed on the side of the expansion opposite the filament. The addition of the plate minimized the field deflection of the generated ions and allowed the experiments to be run with a lower current through the filament, extending its useful life. Hereafter, the ion generation conditions with the metal plate, oxygen as a carrier gas and the filament placed in location 1, will be referred to as ion source A. In contrast, the conditions using the N_2O carrier gas, without the metal plate opposing the electron filament and the filament in location 1, will be referred to as source B. For comparison of the effects on ion generation for these various conditions, the photoelectron energy spectra are given in figure 4.2. The ion generation conditions A and B were chosen because they most strongly accentuated features described in detail in section 4.5.

The atomic oxygen anions, formed in the resulting plasma from either O_2 or N_2O, were presumed to react with isoxazole, resulting in its deprotonation.[77] The anions were then separated according to their masses in a time-of-flight mass spectrometer and interrogated by ~7 ns 355, 306, or 266 nm laser pulses.

The electrons photodetached[13] from the mass-selected anions were projected using a velocity-map[19] imaging[17,50] (VMI) assembly onto a 40 mm diameter position-sensitive dual microchannel plate detector coupled to a P43 phosphor screen. The resulting photoelectron images were recorded using a charge-coupled device camera (Photometrics, Inc., CoolSnap Myo). All images reported here correspond to multiple experimental runs totaling ~10^6

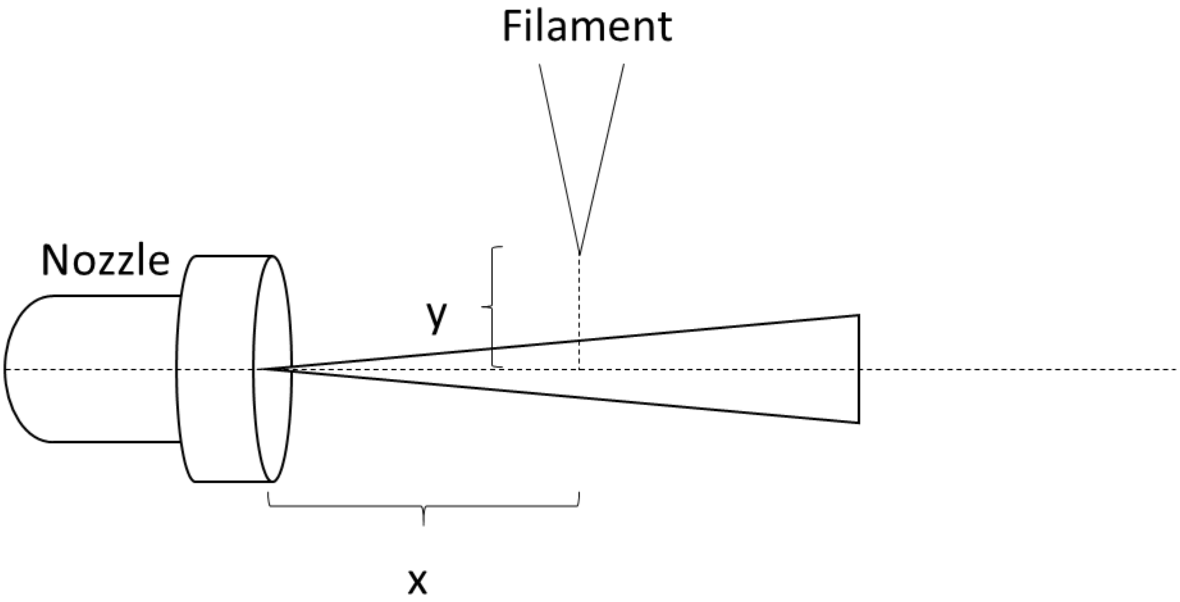

Figure 4.1 Schematic of filament orientation relative to the nozzle for the generation of isoxazolide anions. Small values of X mean the ions have more distance over which to expand and thus cool. The filament location had a large impact on ion generation and the resulting photoelectron energy spectra. This is due to the relative population of isoxazolide isomers generated. See Figure 4.2 for the resulting energy spectra.

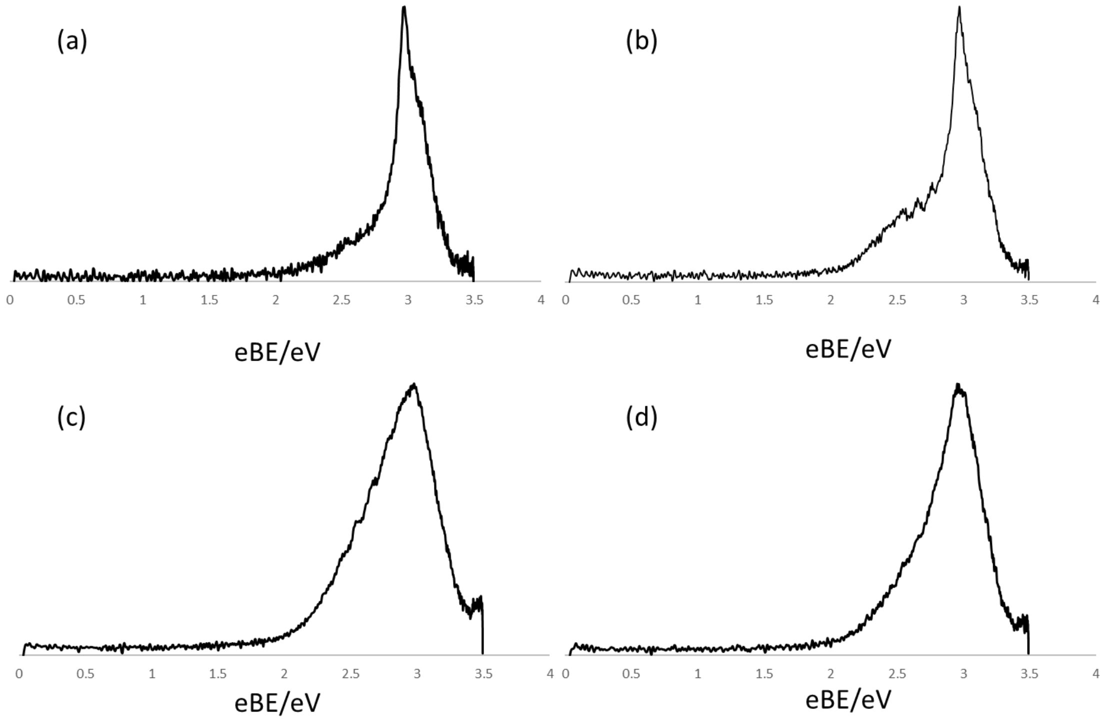

Figure 4.2 Photoelectron energy spectra of the isoxazolide anion. Filament positions are labeled according to the schematic in Figure 4.1. (a) filament position x = 3 cm y = 1.5 cm with N_2O as the carrier gas. (b) filament position x = 3 cm y = 1.5 cm with O_2 as the carrier gas. (c) filament position x = 5 mm y = 3 mm with O_2 as the carrier gas. (d) filament position x = 5 cm y = 1.5 cm with O_2 as the carrier gas. Several other positions were tested with similar results to (c) and (d). The results of (a) and (b) are used as ion generation conditions A and B respectively for the rest of this Chapter.

experimental cycles each. The results were analyzed via an inverse Abel transformation[50] using the BASEX program.[49]

4.3 Experimental Results

The raw photoelectron images of deprotonated isoxazole, collected using ion source A at 266 nm, 306 nm, and 355 nm are presented in Figure 4.3(a)-(c), alongside the corresponding spectra. All photoelectron spectra in this work are plotted versus electron binding energy, eBE = *hv* – eKE, where *hv* is the photon energy and eKE is the electron kinetic energy. Unlike the seemingly similar case of oxazolide, studied by our group previously,[65] no clear vibrational resolution was achieved in this work, with one exception discussed in Section 4.5. The lack of resolved vibrational progressions is due to the naturally congested spectra and overlapping contributions of more than one anion isomer. The experimental resolution itself is similar to the previous work.

All three spectra in Figure 4.3 exhibit a dominant photodetachment transition at ~3 eV. It is usually assumed that the position of a photodetachment band maximum corresponds to the vertical detachment energy (VDE). However, based on the analysis in Sections 4.4 and 4.5, this dominant band is attributed to a mixture of anion isomers; hence the maximum position does not necessarily correspond to the VDE of any particular anion.

The 355 nm spectrum in Figure 1(a) shows a low-eBE shoulder for the dominant spectral band. This shoulder is also discernable, albeit not as clearly, in the 306 and 266 nm spectra in Figures 4.3(b) and (c), respectively. The intensity of the shoulder was observed to change significantly depending on the ion generation conditions. This behavior is consistent with

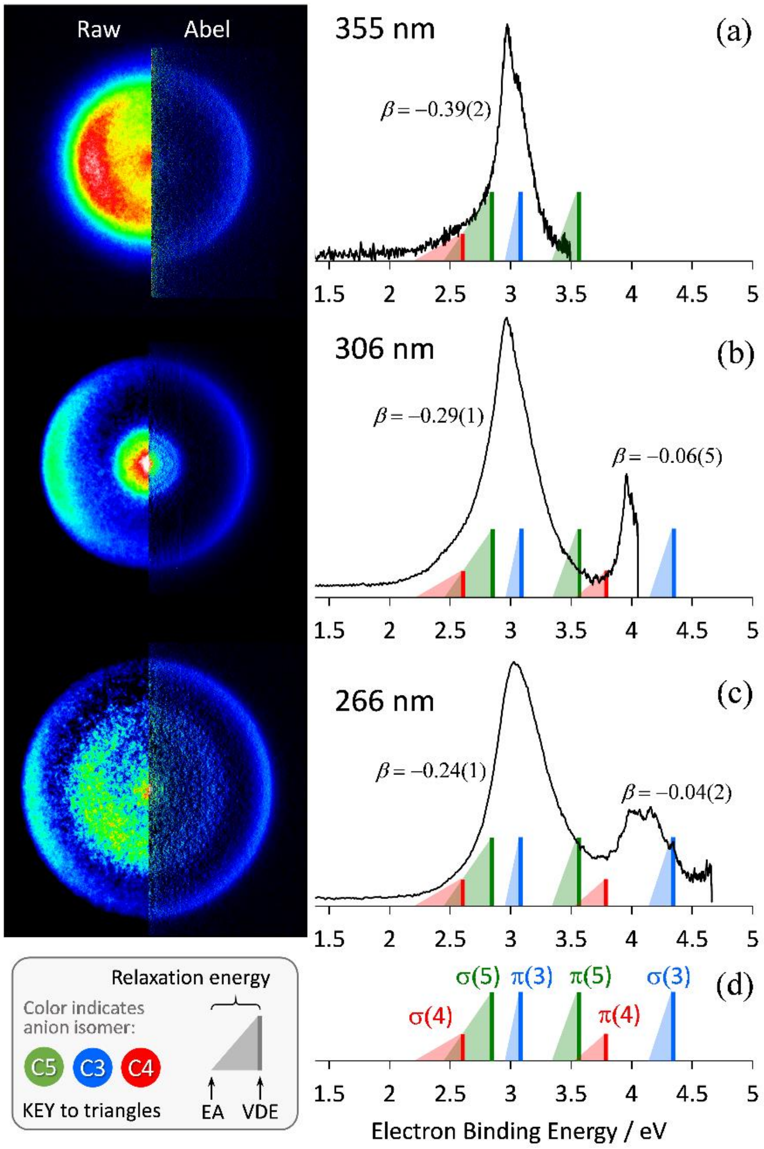

Figure 4.3 Composite raw and Abel-inverted photoelectron images (left and right halves, respectively) and the corresponding photoelectron spectra of deprotonated isoxazole obtained at (a) 355 nm, (b) 306 nm, and (c) 266 nm. The spectrum of triangular graphs in (d), also superimposed for clarity and convenience with the experimental spectra in (a)-(c),

summarizes the results of the EOM-IP-CCSD/aug-cc-pVTZ calculations for the C5-, C3-, and C4-anion isomers, described in Section 4.4. The bold vertical sides of the triangles represent the VDEs of the indicated transitions and should be viewed, collectively, as traditional stick-spectra. The left vertices of the triangles indicate the EAs of the corresponding neutral states. The lengths of the horizontal sides, therefore, correspond to the neutral-radical relaxation energies, serving as an indication of the expected width of the Franck-Condon envelope of each corresponding transition. See Section 4.5 for details.

the presence of more than one anion isomer, whose relative populations vary depending on the ion source conditions. To emphasize this point, Figure 4.4(a) and (b) compares the 355 nm spectra of the ions generated using ion source A and ion source B, respectively. The low-eBE shoulder in Figure 4.4(b) is not only enhanced in relative intensity, compared to Figure 4.4(a), but also shows a partially resolved vibrational progression with an average spacing of 0.11(1) eV or 890(80) cm^{-1}.

As can be seen by visual inspection of the data in Figure 4.3, the photoelectron images exhibit slightly perpendicular photoelectron angular distributions (PADs). The values of the photoelectron anisotropy parameter β corresponding to different photodetachment bands are indicated next to them in the photoelectron spectra. The β values were determined by analyzing the angular dependence of the images, integrated in the energy domain over the full width at half-maximum of the corresponding spectral peaks.[24,49] Compared to other heterocyclic aromatics,[35] little variation of β for different transitions or as a function of eKE is observed in this work. We attribute this, in part, to the spectral overlap of different anion isomers, as discussed in the following Sections.

4.4 Theoretical Modeling

As discussed in the Introduction, the ease of deprotonation in isoxazole is expected to decrease from C5 to C3 to C4 (Scheme 4.1). Past studies showed deprotonation at C5 and C3,[11] and consistent with these observations, the sensitivity of the photoelectron spectra to the ion source conditions in the present work suggests the existence of more than one active deprotonation site, resulting in competing reaction pathways and products. No such sensitivity was noted in the previous work on oxazolide,[65] consistent with the generation of only one anion isomer.

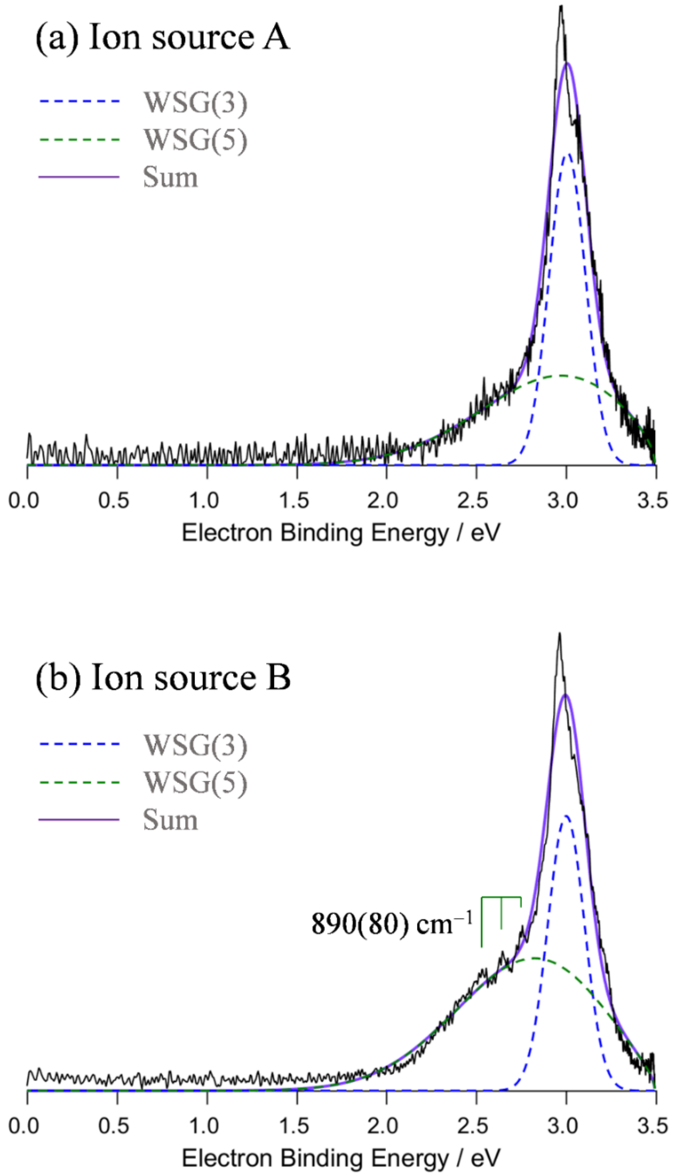

Figure 4.4 The black noisy lines in (a) and (b) represent the experimental photoelectron spectra of deprotonated isoxazole collected using ion source conditions A and B, respectively. The dashed blue and green curves in each case represent the Wigner-scaled Gaussian (WSG) basis functions WSG(3) and WSG(5), respectively, representing the π(3)

and σ(5) transitions, as defined in Section 4.5 and Figure 1(d), used to fit to the experimental spectra. The solid purple curve in each case is the resulting least-squares fit to the data. The three-pronged comb in (b) indicates a vibrational progression, partially-resolved in the experimental spectrum, attributed to an in-plane ring-distortion mode.

To assist in the interpretation of the results, we carried out geometry optimizations and selected potential energy scans for the deprotonated isoxazole anions, as well as the corresponding neutral radicals. The calculations were performed using the QChem software package.[78] The coupled-cluster theory with single and double excitations (CCSD) was used for all anion geometry optimizations. The anion VDEs and neutral electron affinities (EA) were calculated using the equation-of-motion (EOM) ionization-potential (IP) formalism, combined with the coupled-cluster theory.[79] For each stable isomer of the anion, the VDEs were determined for transitions to two lowest electronic states of the corresponding neutral radical: the ^{2}A′ (σ-radical) and ^{2}A″ (π-radical) states. The respective VDE(σ) and VDE(π) values were obtained from single-point EOM-IP-CCSD calculations for optimized anion structures, removing the highest-energy appropriate-symmetry electron from the closed-shell anion reference.

Attempts to optimize the neutral structures at the CCSD level of theory resulted in significant spin contamination ($\langle S^2 \rangle \approx 1.1$, compared to expected 0.75) and were therefore deemed unreliable. Instead, the geometries of the ground and first excited electronic states of the neutral radicals were optimized using the unrestricted EOM-IP-CCSD method. Each neutral state was accessed by removing an appropriate-symmetry electron from the closed-shell anion reference and the geometry was optimized by following the potential gradient of the target state. The adiabatic electron affinities or adiabatic electron attachment/binding energies were calculated as energy differences between the respective geometry-optimized neutral and anion states. For brevity, both the electron affinities (for the ground states) and the adiabatic attachment energies (for the excited states) are hereafter referred to as electron affinities of the corresponding states. All CCSD and EOM-IP-CCSD calculations reported here employed the aug-cc-pVTZ basis set. Where noted, additional quick surveying calculations and potential energy scans were performed using the B3LYP density functional with the aug-cc-pVDZ basis set.

The results of the calculations are summarized in Figure 4.5 and Table 4.1. Figure 4.5 shows the anion structures and their relative energetics, with the three panels corresponding to isoxazole deprotonation at the C5, C3, and C4 positions, in the order of decreasing acidity. The C5, C3, and C4 panels are labeled in green, blue, and red. The same colors are used in Figures 4.3 and 4.4 to color-code the spectral assignments and model spectra. Table 4.1 summarizes the complete geometric parameters of the optimized anion and ground-state neutral structures. Vibrational frequency calculations were used to verify that the anion structures shown correspond to true potential minima.

As expected, the calculations show that C4 deprotonation is less favorable than C5, by 0.30 eV. This value was determined by comparing the CCSD energies of the optimized C5- and C4-isoxazolide structures. It is impossible to give a corresponding value for isoxazole deprotonation at the C3 position, because this process triggers the dissociation of the N−O bond, followed by the opening of the ring. Relaxed potential energy scans with respect to the C4–C3–N bond angle (B3LYP/aug-cc-pVDZ) showed no barrier to the ring opening in C3-isoxazolide, contrasting the C5 and C4 deprotonation pathways, both of which keep the ring intact. Since the immediate product of C3 deprotonation, C3-isoxazolide, is not a stationary structure, it does not possess an energy eigenvalue. This is

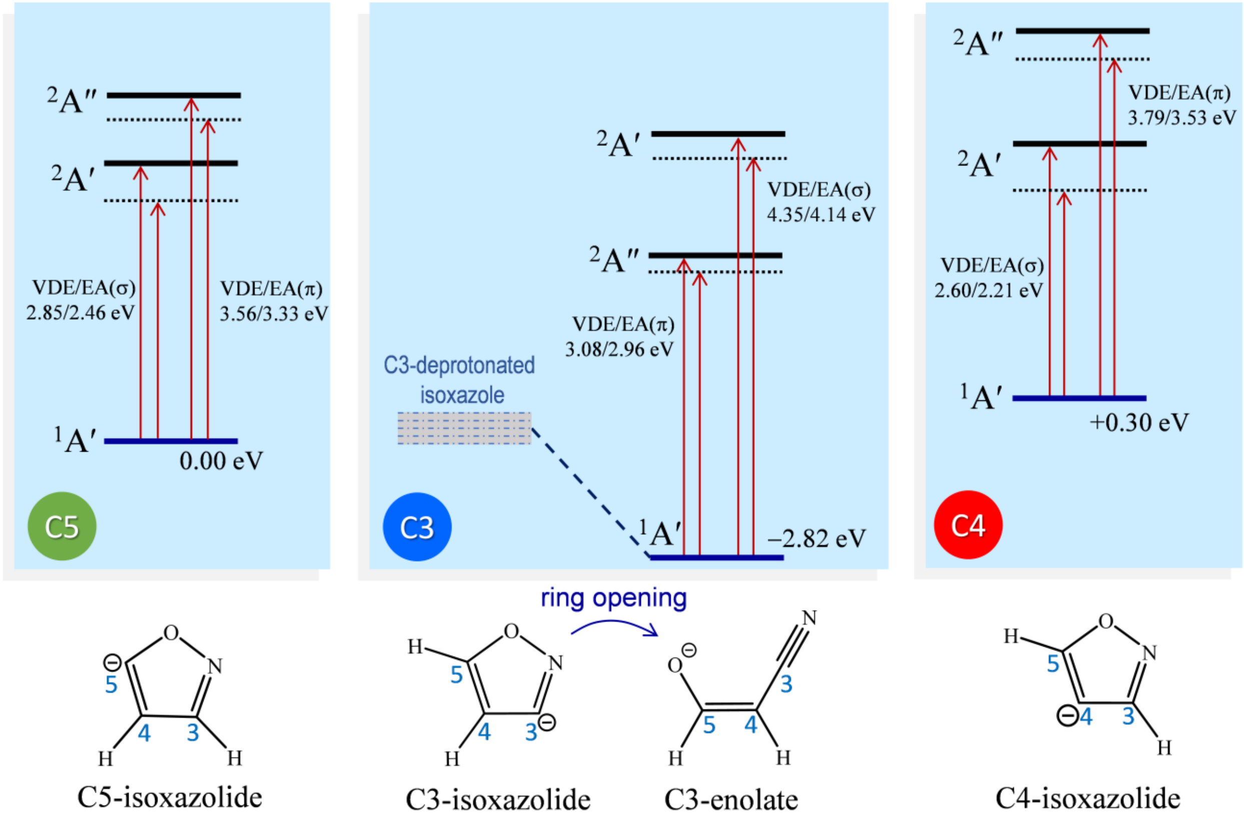

Figure 4.5. Possible isomers of the isoxazolide anion formed by the removal of H^+ from isoxazole. All relative energy values are calculated at the CCSD and EOM-IP-CCSD levels of theory with the aug-cc-pVTZ basis set. The dashed energy levels for the neutral (doublet) states correspond to the optimized radical structures, while the solid lines represent the corresponding neutral-state energy levels accessed in vertical photodetachment of the anions.

Table 4.1 Geometric parameters of the equilibrium anion and neutral structures resulting from the deprotonation or H-dissociation of isoxazole at the C5, C3, or C4 positions, respectively. The anion structures are shown at the bottom of Figure 4.6. Geometry optimizations were carried out at the CCSD level of theory with the aug-cc-pVTZ basis set. The bond lengths are given in Angstroms and bond angles in degrees.

	C5-isoxazolide	C5-isoxazolyl	C3-enolate anion	C3-enolate radical	C4-isoxazolide	C4-isoxazolyl
O–N	1.423	1.425	n/a	n/a	1.387	1.394
N–C3	1.307	1.306	1.166	1.161	1.315	1.307
C3–C4	1.418	1.429	1.414	1.405	1.453	1.417
C4-C5	1.395	1.350	1.399	1.451	1.365	1.345
C5–O	1.372	1.304	1.245	1.217	1.388	1.347
C3–H	1.082	1.077	n/a	n/a	1.085	1.076
C4–H	1.079	1.072	1.080	1.081	n/a	n/a
C5–H	n/a	n/a	1.113	1.098	1.082	1.075
∠O-N-C3	103.3	104.8	n/a	n/a	104.5	106.5
∠N-C3-C4	112.6	113.3	177.6	178.5	117.2	110.0
∠C3-C4-C5	107.0	100.3	123.8	121.1	96.5	105.8
∠C4-C5-O	104.0	114.8	129.9	123.0	115.7	108.7
∠N-C3-H	118.1	118.1	n/a	n/a	115.6	119.6
∠C3-C4-H	126.6	130.1	117.3	118.4	n/a	n/a
∠C4-C5-H	n/a	n/a	112.1	115.7	133.0	134.7

indicated schematically by a shaded energy band representing C3-isoxazolide in Figure 4.5.

As shown at the bottom of Figure 4.5, the opening of the ring in C3-isoxazolide does produce an equilibrium anion structure, whose IUPAC name is (Z)-2-cyanoethen-1-olate. We will refer to it, for brevity, as C3-enolate, where the prefix indicates its origin from C3 deprotonation of isoxazole. There is no information in the literature about previous studies of this anion. Allowing fleeting liberty with the nomenclature in referring to C3-enolate as the *cis* (with respect to the C4=C5 bond) isomer, it should be noted that the corresponding *trans* form, (E)-2-cyanoethen-1-olate (not shown), is 0.095 eV (B3LYP/aug-cc-pVDZ) more stable than the *cis* C3-enolate structure shown. However, a potential energy scan with respect to the C4=C5 torsion angle (B3LYP/aug-cc-pVDZ) indicates a 1.3 eV barrier separating the *cis* and *trans* anions, consistent with the π bonding character included in the C4=C5 bond. Therefore, we deem the *trans*-C3-enolate anion to be inaccessible in the present experiments and make no further reference to it here.

As seen in Figure 4.5, the ring opening from C3-isoxazolide to C3-enolate results in significant stabilization of the anion. According to CCSD/aug-cc-pVTZ, C3-enolate is 2.82 eV more stable than C5-isoxazolide. However, the final-state energetics should not be taken to indicate that the C3 species must dominate the anion population. The formation of all anion isomers involves an initial deprotonation step, which is followed by a downhill ring-opening in the C3 case only. Since little coupling can be conceived between the final C3, C4, and C5 structures, their relative populations are determined by the relative ease of the initial C3 vs. C4 vs. C5 deprotonation steps. Since the acidity considerations indicate that C5 deprotonation is slightly more favorable than C3 (initially), the formation of C5-

isoxazolide may be correspondingly more efficient than the formation of the (ultimately) more stable C3-enolate form. Considering the energetics of an electron-impact ionized plasma, even the C4 deprotonation in our experiment cannot be ruled out *a priori*.

The neutral state energies are also indicated in Figure 4.5 based on the EOM-IP-CCSD results. For each anion isomer, the two lowest neutral electronic states are described: one corresponding to the σ radical (^{2}A′ state) and one to the π radical (^{2}A″ state). (In this work, the σ and π designations refer to the orbital nodal character with respect to the molecular plane; they are not used in the rigorous spectroscopic sense associated with the projection of orbital angular momentum on an internuclear axis.) In Figure 4.5, each radical state is represented by two energy levels: one (shown by solid horizontal lines) is obtained via a vertical detachment transition from the relaxed anion structure and the other (dashed horizontal lines) corresponds to a relaxed neutral geometry. For each neutral state, the energy difference between the "solid" level and the optimized anion structure corresponds to the anion VDE, while the difference between the "dashed" level and the optimized anion structure is the neutral's EA. The difference between the "solid" and "dashed" neutral energy levels, i.e. (VDE − EA), is the neutral state's relaxation energy.

The ring-closed C4- and C5-isoxazolide anions, as well as the ring-open C3-enolate, are a closed-shell ^{1}A′ species. The completely filled HOMO and HOMO−1 orbitals of each of the anion isomers are shown in Figure 4.6. The ground states of neutral C5- and C4-isoxazolyl correspond to σ radicals ($X\,^2$A′) formed by the ejection of an electron from the a' HOMO of the respective anions. As expected, these HOMOs have significant C5/C4 (respectively) sp^2 hybrid character. The corresponding canonical orbital of the C5/C4-isoxazolyl radical would combine with the 1s orbital of H to form the C5/C4-H σ bond in the isoxazole molecule. The first excited states of C5- and C4-isoxazolyl are π radicals ($A\,^2$A″) formed by the ejection of an electron from the *a″* HOMO−1 of the corresponding anions.

The HOMO and HOMO-1 of ring-closed C3-isoxazolide (not shown) are similar to their C4 and C5 counterparts in that they too are σ (*a′*) and π (*a″*) in their respective characters, with the HOMO having a large contribution from the C3 sp^2 hybrid. However, the ordering of the orbitals changes upon the opening of the ring, with the π orbital becoming the HOMO of the C3-enolate anion. The immediate implication of this change is that the lowest-energy photodetachment transition in C3-enolate accesses the π-radical ground state of the neutral, while the σ-radical becomes an excited state, as indicated in Figure 3. The σ-character HOMO−1 of C3-enolate (Figure 4.6) includes no sp^2 hybrid contribution from the deprotonated carbon, C3. In fact, the C3 atom in C3-enolate is in the *sp* hybridization state. Instead, this *a′* MO includes dominant contributions from the C5 (not C3) atom sp^2 hybrids, coupled with the in-plane *p* orbital on the oxygen atom. Overall, the MO has, predominantly, a clear *d*-like character, qualitatively similar to the π_g^* HOMO of O_2^-.

As seen in Figure 3, the relaxation energies, VDE − EA, of the σ radical states are consistently larger than those of the π radicals for each of the three isomers. This is to be expected, because the removal of an electron from an in-plane MO results in a greater distortion of the molecular geometry compared to the removal of an electron from an out-of-plane MO. We further note that the slightly negative anisotropy values reported in Figure 1 are consistent with the detachment from all types of orbitals illustrated in Figure 4.4. Past studies and analysis using the *s-p* mixed character model predicted moderately negative β

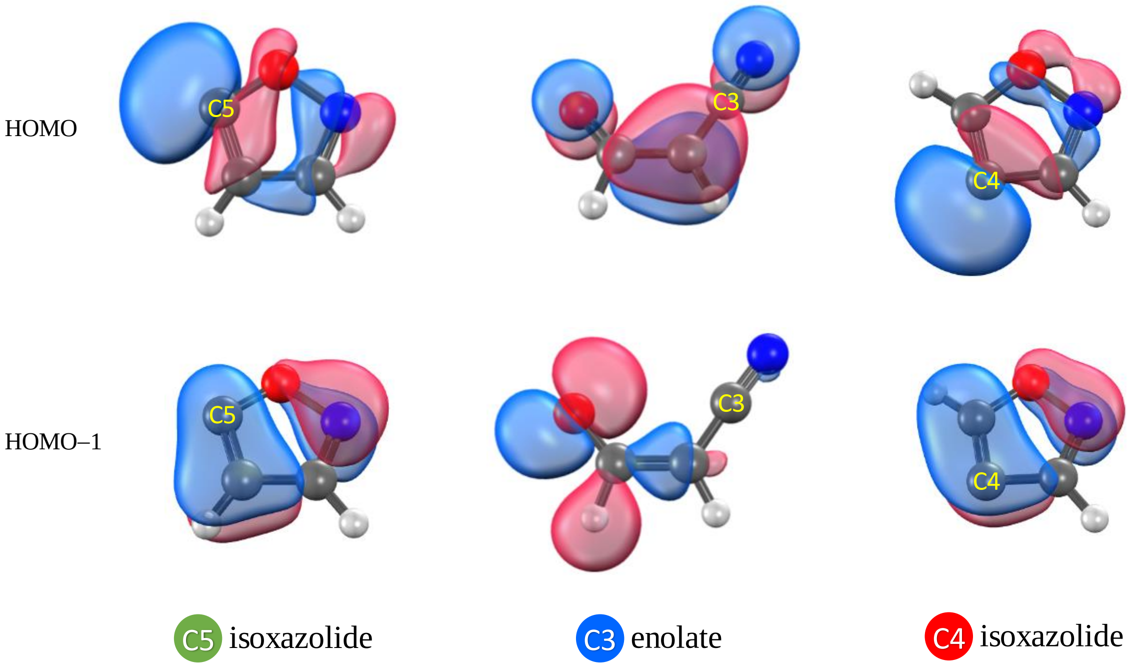

Figure 4.6 The HOMO (top row) and HOMO-1 (second row) of each of the anion isomers discussed in this work, calculated at the CCSD level of theory with the aug-cc-pVTZ basis set. The surfaces shown correspond to an isovalue of 0.10.

values in the detachment from in-plane σ orbitals of similar heterocyclics with significant sp^2 hybrid character.[16,35] Similarly, negative values of the anisotropy parameter should be expected based on qualitative symmetry considerations in the detachment form π type MOs,[23] as well as from *d*-like MOs,[16,30,31,80] similar to C3-enolate's *a′* HOMO−1. Hence, in the deprotonation of isoxazole, we have relatively small expected anisotropy variation for different photodetachment transitions, combined with the co-existence of different anion isomers with partially overlapping photoelectron spectra. It is not surprising, therefore, that little quantitative analysis of the PADs could be carried out in this work, beyond the general qualitative conclusion about the agreement of the experimental observations with the model predictions.

4.5 Discussion

The experimental images and spectra in this work are assigned to a combination of the anion isomers resulting from the deprotonation of the precursor isoxazole molecule. The past studies[11] provided evidence of isoxazole deprotonation at C5 and C3 positions, but not at C4. The ion-generation conditions in our experiment are drastically different and the excitation energies existing within the electron-impact ionized plasma in our ion source may be sufficient to activate deprotonation even at the most unfavorable C4 position. There is no contradiction between this conclusion and the past study of oxazole, where deprotonation was observed at only one position. Oxazole and isoxazole are chemically distinct molecules. Although both are weak bases, the pK_a values of their respective conjugate acids (i.e. protonated, rather than deprotonated molecules) are significantly different: 0.8 for H^+·oxazole, compared to −3.0 for H^+·isoxazole.[81] Similarly, there is no reason to expect the deprotonation behaviors of the two molecules to be identical.

The past oxazole work relied on definitive mass-spectrometric data for the deuterated form of the compound to draw the conclusion about its selective deprotonation.[65] Similarly, concrete experimental evidence would be needed to rule out any deprotonation pathways in isoxazole. The available evidence does not provide sufficient basis for excluding any of the pathways. To the contrary, the observed changes in the spectra depending on the ion source conditions point to an opposite conclusion: that there are indeed multiple active deprotonation pathways in isoxazole within the electron-impact-ionized plasma.

To facilitate the spectral assignments, the VDE and EA values from Figure 4.5 are also indicated in Figure 4.3, using specifically designed triangular graphs superimposed with the experimental spectra. The graphs follow the isomer color scheme adopted throughout: green for the anion resulting from C5 deprotonation of isoxazole, blue for C3, and red for C4. Two triangular graphs are shown for each isomer in Figures 4.3(b) and (c): one for each of the two lowest photodetachment transitions, accessing the σ and π radical states, for a total of six transitions. In Figure 4.3(a), two of the higher-energy transitions are not shown, because they fall too far outside the photon energy range. The key to the energetic triangles is given in Figure 4.3(d). For example, the σ(5) label corresponds to the $X^1\mathrm{A}' \rightarrow X^2\mathrm{A}'$ transition in C5-isoxazolide, producing the C5-isoxazolyl σ-radical. The bold vertical sides of the triangles should be viewed as traditional stick-spectra, indicating the VDEs of the transitions. The position of the left vertex of each triangle indicates the adiabatic electron affinity of the corresponding neutral state. The length of the horizontal side, corresponding to the difference between the VDE and the EA is, therefore, the relaxation energy of the neutral radical. The relaxation energy serves as an indication of the expected width of the Franck-Condon envelope of the corresponding transition. In comparing the experimental spectra in Figure 4.3 to the spectrum of the calculated triangles, one should keep in mind that the EOM-IP-CCSD calculations achieve better accuracy in describing the lowest-energy photodetachment transitions, compared to the excited states. Finally, while we cannot predict either the relative isomer populations or the corresponding photodetachment cross-sections, we do expect, on energetic grounds, the contribution of the C4 anion isomer to be smaller than that of either C5 or C3. This expectation is indicated by the reduced height of the C4 triangles in Figure 4.3.

Comparing the experimental and theoretical results in Figure 4.3, we conclude that none of the three possible anion isomers can be definitively excluded from consideration. As discussed above, the coexistence of the C5 and C3 isomers is expected, based on the past results,[11] deprotonation energetics, and the observed dependence of the spectra on the ion source conditions in this work. However, even the highest-energy C4 isomer cannot be excluded based on the available data. In particular, the long low-eBE shoulder of the main photodetachment band appears consistent with σ photodetachment of a combination of the C5 and C4 isoxazolide isomers, i.e. transitions $\sigma(5)$ and $\sigma(4)$. The more pronounced band peaking at about 3 eV is attributed to the lowest-energy transition in C3-enolate, $\pi(3)$. The broader right shoulder of the dominant peak in the 306 and 266 nm spectra is attributed to the second transition in C5-isoxazolide, $\pi(5)$. This shoulder is most pronounced at 266 nm and least visible at 355 nm, consistent with the near-threshold Wigner suppression of the electronic part of the photodetachment cross-section.[28,56] The separate band, appearing at higher energies in the 306 and 266 nm spectra and peaking at eBE > 4 eV in the latter, is assigned to the second transition in C3-enolate, $\sigma(3)$, but the $\pi(4)$ transition may also be contributing to the lower-eBE shoulder of this band.

To examine the competition of the anion isomers, we modelled the 355 nm photoelectron spectra obtained using different ion-source conditions. The results are in Figure 4.4. As seen by comparing the experimental spectra in (a) and (b), the low-eBE shoulder in the source-A spectrum is smaller, relative to the dominant peak, compared to the similar shoulder in the source-B spectrum. These spectral variations are consistent with the existence of competing deprotonation pathways in the parent isoxazole molecule, yielding coexisting anion isomers with varying relative populations.

In modeling these spectra, we rolled the C5 and possible C4 contributions into a single model band, corresponding, predominantly, to the C5 isomer (effectively neglecting the C4 contribution). We then modeled the experimental spectra as superpositions of two Wigner-scaled Gaussians (WSG), one—WSG(5)—corresponding to C5-isoxazolide and one—WSG(3)—to C3-enolate. A WSG is a normalized Gaussian function of eBE, multiplied by an $\mathrm{eKE}^{1/2} = (h\nu - \mathrm{eBE})^{1/2}$ pre-factor. The Gaussians simulate the Franck-Condon envelopes of the transitions, with the maximum position corresponding to the VDE, while the pre-factor accounts for the near-threshold scaling of the electronic cross-sections. The form of the scaling function chosen corresponds to the Wigner law[28] with the $l = 0$ value of the orbital angular momentum quantum number of the outgoing free electron. Granted, the final state in the observed transitions is a superposition of partial waves with different l values. However, in the low-eKE regime, where the Wigner scaling is most important, the *s* partial waves will dominate (assuming they are allowed by the selection rules). Therefore, in the absence of detailed information about the partial-wave composition, the above scaling function is most appropriate, if only approximate. This approach to modeling of photoelectron spectra has been tested by our group on other systems in several previous publications.[82,83]

In each case shown in Figures 4.4(a) and (b), a superposition of WSG(5) and WSG(3) model functions was fit to the experimental spectra, with their relative coefficients, Gaussian maximum positions (VDEs), and Gaussian widths treated as adjustable parameters. In each case, the two WSG functions, as well as their superposition, are shown in the figure, superimposed with the experimental spectrum. For the lower-eBE function, WSG(5), the fits returned VDE = 2.97 eV and 2.83 eV for ion sources A and B, respectively. These values, giving 2.90 eV on average, should be compared to VDE(σ) = of 2.85 eV calculated for C5-isoxazolide. The possible contribution of C4 is expected to be smaller and mostly important at the lower-eBE shoulder of the transition rather than near its peak; it may, however, be partially responsible for the variation in the above fit VDE values. The second model function, WSG(3), describing the π-radical transition in C3-enolate, gives VDE values of 3.01 eV and 3.00 eV in Figures 4.4(a) and (b), respectively, to be compared to VDE(π) = 3.08 eV calculated for C3-enolate. Based on these fits, we determine the VDE values for C5-isoxazolide and C3-enolate to be 2.90(7) eV and 3.00(1) eV, respectively.

In both Figures 4.4(a) and (b) the Gaussian part of WSG(3) is narrower than that of WSG(5). This is consistent with the smaller neutral relaxation energy associated with the π(3) transition compared to σ(5), as seen in the theoretical results summarized in Figures 1 and 3. Turning to the relative weights of the different isomers, the ratio of the WSG(5) and WSG(3) coefficients is 1.48 in Figure 4.4(a), compared to 1.94 in Figure 4.4(b). Without knowing the relative magnitudes of the photodetachment cross-sections of different isomers, it is impossible to translate these figures into the relative isomer populations. However, it can be stated with confidence that the fractional population of C3-enolate in ion source A is approximately 30% larger than in ion source B. The other ion generation conditions described by Figure 4.2 show the sensitivity of fractional isomer population to these conditions.

At low energies, the spectrum in Figure 4.4(b) reveals a faint signature of a vibrational progression attributed to C5-isoxazolide. This progression is less discernable in Figure 4.4(a), because the C5 spectrum there is overwhelmed by the larger contribution of C3-enolate. The 0.11(1) eV or 890(80) cm^{-1} spacing between the vibrational peaks agrees well with the 892 cm^{-1} frequency of an in-plane ring-distortion mode in C5-isoxazolyl, predicted based on the B3LYP/aug-cc-pVDZ harmonic frequency calculation. It also agrees well with the same-frequency, 890(80) cm^{-1}, vibrational progression observed in the photoelectron spectrum of C2-oxazolide, assigned to a similar in-plane ring-distortion mode in the oxazolyl radical.[65]

Finally, we comment that the observed VDE of C5-isoxazolide, 2.90(7) eV, is sizably larger than the corresponding value for C2-oxazolide, 2.66(2) eV. A similar difference applies to the adiabatic EAs of the corresponding isoxazolyl and oxazolyl radicals. Although the EA of isoxazolyl could not be determined reliably from the experimental data in this work, the high-level calculations place this value for the C5-radical (corresponding to the most acidic deprotonation pathway) at 2.46 eV (Figure 4.5), in general agreement with the experimental spectra. This is to be compared to the experimentally determined EA of C2-oxazolyl, 2.21(2) eV.[65] Overall, a quarter-of-an-electron-volt increase in electron binding energies in deprotonated isoxazole, compared to oxazole, may explain the multiple active deprotonation pathways in isoxazole, contrasting the sole pathway observed in oxazole.

4.6 Summary and Conclusions

Deprotonation of isoxazole can occur at three distinct positions within the molecule. Deprotonation at the most acidic (C5), as well as the least acidic (C4) positions yields the respective C5- and C4-isoxazolide anions, while the reaction at the intermediate-acidity C3 site leads to a cleavage of the O−N bond and an opening of the ring in the anion. The anion photoelectron spectra of deprotonated isoxazole are assigned to a mixture of predominantly C5-isoxazolide, with a VDE of 2.90(7) eV, and C3-enolate, with a VDE of 3.00(1) eV, with a possible but less significant contribution from C4-isoxazolide. The former value, for C5-isoxazolide, is sizably larger than the VDE = 2.66(2) eV of C2-oxazolide, formed via the most acidic and the sole observed deprotonation pathway in oxazole. In contrast to oxazolide, the relative intensities of the isoxazolide spectral bands exhibit sensitivity to the ion source conditions, giving evidence of competing and varying contributions of the different deprotonation pathways. The lowest energy photodetachment transitions in the C5- and C4-isoxazolide anions access the σ-radical ($X\,^2\mathrm{A}'$) ground states of C5- and C4-isoxazolyl, respectively, while the ground-state neutral derived from ring-open C3-enolate is a π radical ($X\,^2\mathrm{A}''$).

CHAPTER 5: CHEMISTRY OF THE BREAKING BOND

5.1 Introduction

Bond breaking is an experimentally and theoretically challenging problem. The electronic structure of a dissociating chemical bond is transient and multi-configurational. In this Chapter, we focus on chemical bonds stretched far beyond their equilibrium lengths, characterized by a diradical (two unpaired electrons) electronic structure exhibiting interactions between two radical centers.[84] This interaction gives rise to a manifold of nearly degenerate electronic states with multi-configurational wavefunctions due to the many ways of combining the orbital contributions and spins of the electrons. Nearly broken chemical bonds are usually not found in stable structures that can be easily probed. We access these states by photodetaching an electron from a stable radical anion[85,86] which transitions to a diradical neutral, where the fragment radicals cannot separate completely but remain constrained by intact molecular geometry.

A previous study[87] from our group used oxazole as the molecular framework to access a diradical interaction of a nearly broken covalent bond. Oxazole undergoes bond fission upon electron attachment as shown in Figure 5.1 where the excess charge resides primarily on the oxygen.[7,8] Photodetachment of an electron is a fast process, which does not allow time for relaxation of the molecular geometry. This means the energy spectrum of the neutral ring-opened oxazole is measured at the geometry of the anion, which leaves the two radical centers ~3 Å apart. The diradical interaction acts as a stretched covalent bond. Additionally, the oxazole anion was also shown to undergo internal rotation about the C-

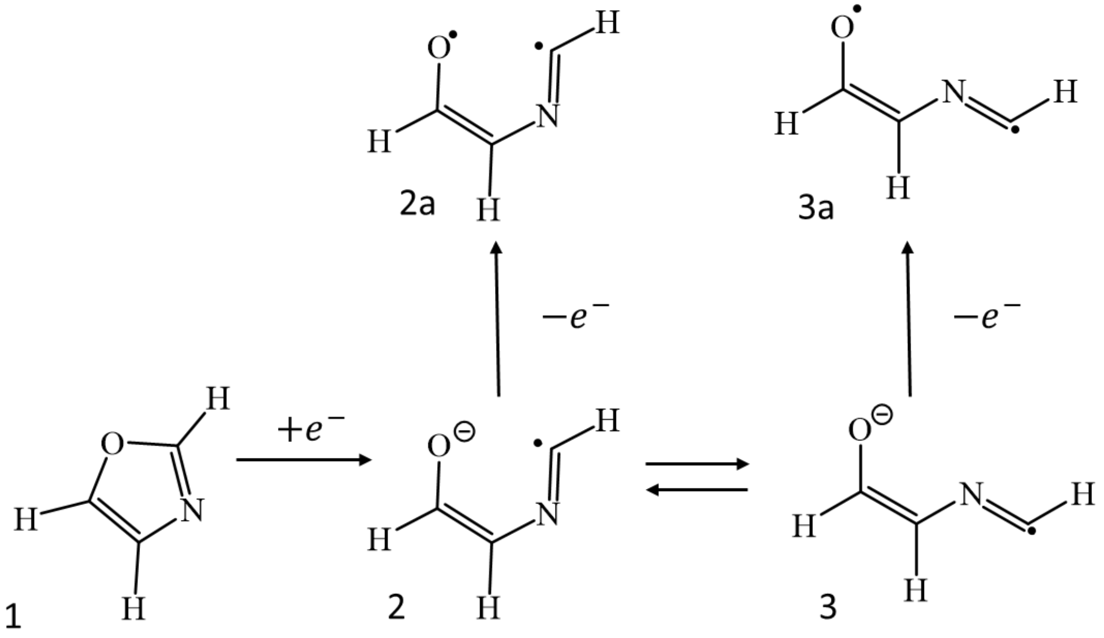

Figure 5.1 Electron attachment and photodetachment pathways of oxazole. 1: closed-shell oxazole. 2 and 3: the cis and trans forms of the ring-open oxazole anion. 2a and 3a: the cis and trans ring-open neutral diradical structures.

N bond which moves the carbon radical much further from the oxygen.[87] Oxazole anion exists as a superposition of these two *cis* and trans structures. Electron detachment from the t*rans* structure leaves a neutral diradical, but the original bond fragments are now far apart.

In the present work, we contrast the ring-opening of oxazole with a similar chemistry in isoxazole. Oxazole and isoxazole are distinct chemical species. As depicted in Figure 5.2, electron attachment to isoxazole also results in ring opening in the anion, but it is the O–N bond rather than an O–C bond that is dissociated in this case[11]. Just as with oxazole, the excess electron in the ring-open isoxazole anion is located primarily on the oxygen atom and photodetachment leads to a neutral diradical with the interaction centers ~3 Å apart. However, isoxazole has a π-conjugated system across the carbon atoms that form the molecular framework keeping the radical centers close. This dramatically increases the energy barrier of internal rotations from a *cis* to a *trans* structure. A potential energy scan done with the Q-chem 5.1[69] software package at the B3LYP/aug-cc-pVDZ level of theory showed a 1.14 eV barrier for this rotation. Each of these states are already multi-configurational and nearly degenerate. With this energy barrier blocking the internal rotation, the number of states probed decreases significantly creating a less convoluted spectrum.

5.2 Experimental and Theoretical Methods

Unlike isoxazolide, the spectrum of isoxazole was not particularly sensitive to the ion generation conditions. The generation conditions used are described in detail in Chapter 4 as ion generation condition A, but without the 5x5 cm metal plate opposite the electron cannon. Both anions were obtained simultaneously by expanding a neutral isoxazole

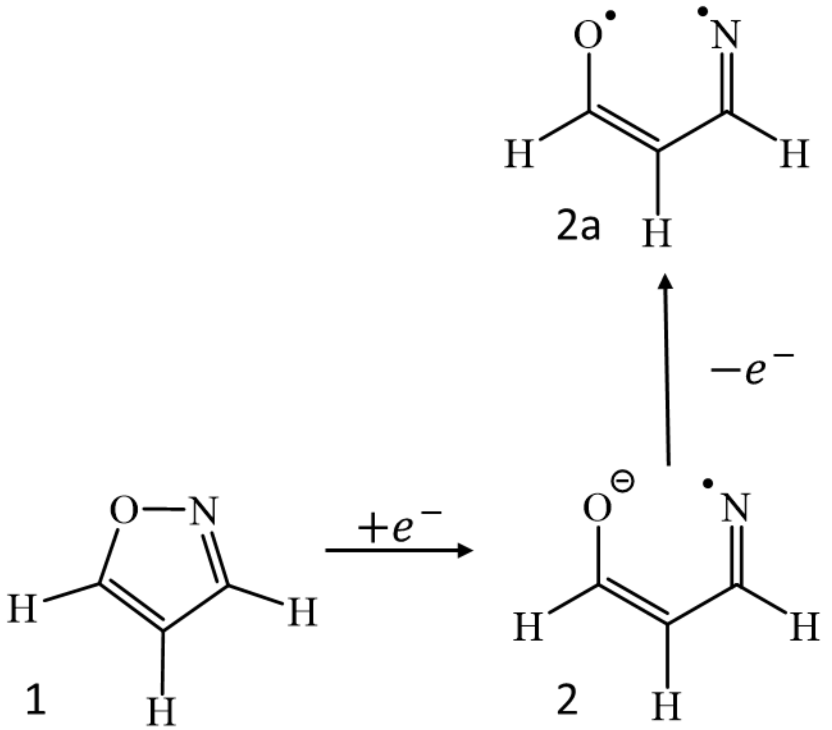

Figure 5.2 Electron attachment and photodetachment pathways of isoxazole. 1: closed-shell oxazole. 2: the *cis* and *trans* form of the ring-open isoxazole anion. 2a: the *cis* and *trans* ring-open neutral diradical structure.

precursor seeded in O_2 gas through a pulsed supersonic nozzle. The precursor isoxazole vapor was picked up from the liquid sample (99%; Sigma Aldrich, Inc.) kept at ambient room temperature. Photoelectron images were collected at 355 nm, 306 nm, and 266 nm.

Electronic-structure optimization calculations were carried out at the CCSD level of theory with the aug-cc-pVTZ basis set, using the Q-Chem 5.1[69] software package. Equation-of-motion (EOM) methods[79,88,89] were combined with coupled-cluster theory. The EOM ionization potential (IP) methodology[79] was used to access the low-lying electronic states of the neutral by removing an electron from the anion reference. Conversely, the EOM electron affinity (EA) method was used to generate the anion state by adding an electron to the closed-shell singlet reference of the neutral structure. Finally, EOM spin-flip (SF)[88] calculations were used to determine the energy gaps within the manifold of the singlet and triplet diradical states of the neutral.

5.3 Experimental Results

The photoelectron images collected at 355, 306, and 266 nm for isoxazole anion are shown in Figure 5.3. Alongside them are the corresponding photoelectron spectra plotted *versus* electron binding energy (eBE).

The spectra are broad and congested, as expected due to the nearly degenerate states formed by a dissociating covalent bond. The floppy structure of the ring-open anion also contributes to the broadness of the spectra. Despite this and in contrast to oxazole[87], the peaks in the isoxazole spectra are well resolved. The vertical detachment energies (VDEs) of the peaks are best defined using the 266 nm spectrum due to low eKE threshold scaling, with energies of 2.64(1) eV and 2.95(2) eV. The high eBE feature in the 355 nm spectrum

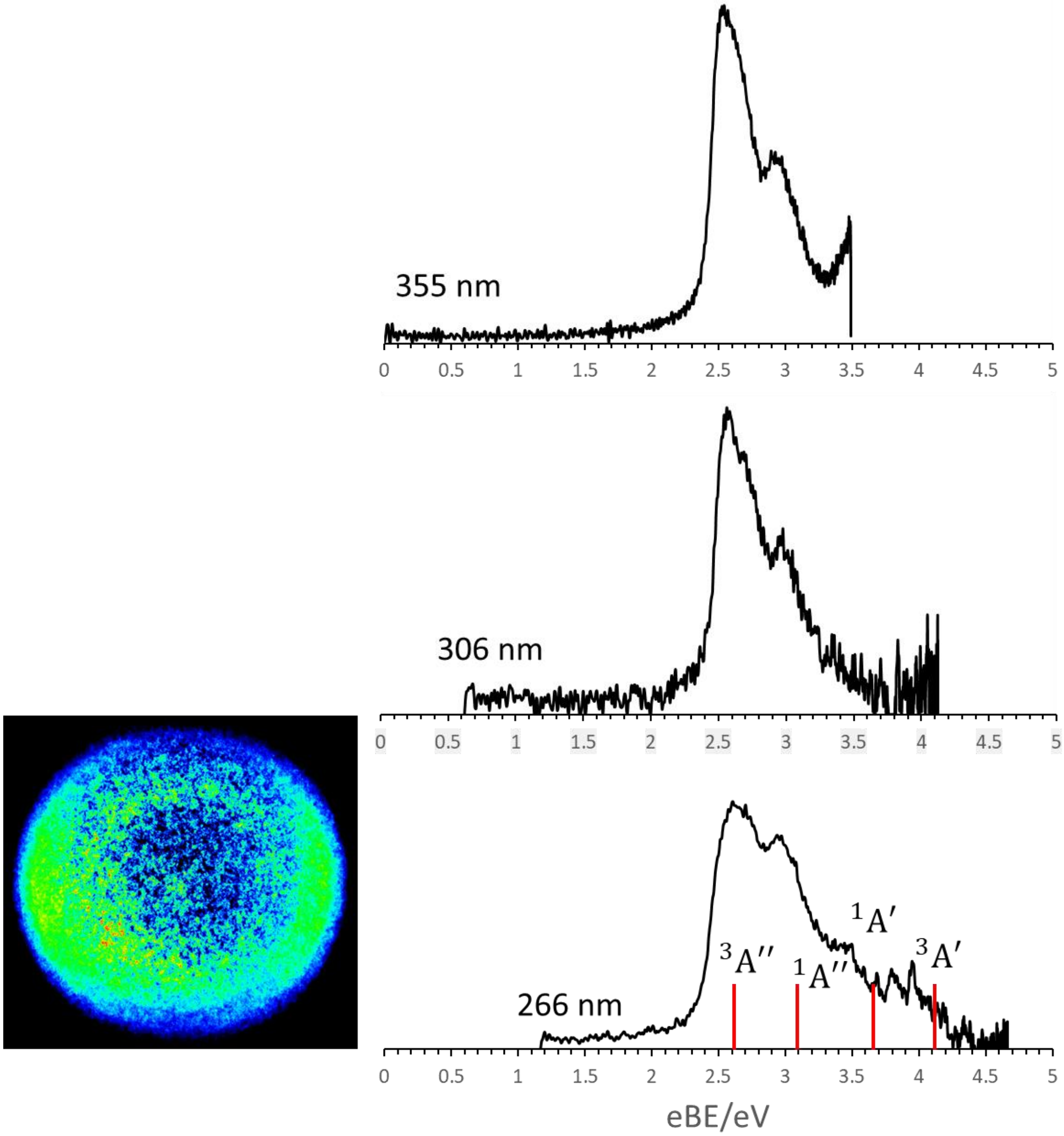

Figure 5.3 Experimental results and assignment. The 266 nm photoelectron image and complete 266, 306, and 355 nm photoelectron spectra of ring-opened isoxazole. The stick spectrum in red is based on the calculations summarized in Figure 5.4

is due to autodetachment. The 266 nm spectrum also shows possible excited state in the range of 3.6 eV − 4.0 eV.

5.4 Discussion

The ring-opened isoxazole anion in its ground state is doublet with the nominal electron configuration $^2\mathrm{A}'$:…$(15\mathrm{a}')^2(3a'')^2(16a')^1$. The antibonding character of the $16a'$ orbital with respect to the O-N bond is responsible for the opening of the ring in the anion. As shown in Figure 5.4 the lowest energy vertical transition to the neutral is a triplet state, which is close in energy to an open-shell singlet state. Both of these states correspond to an electron being detached from the out-of-plane π orbital $3a''$. Electron detachment from out-of-plane orbitals have little impact on the structure of the molecule and thus the geometry of the triplet and open-shell singlet are expected to be similar to the anion geometry. The minimum of the closed shell-singlet state $^1\mathrm{A}'$:…$(15\mathrm{a}')^2(3a'')^2(16a')^0$ corresponds to the relaxed cyclic structure with an intact O-N bond. The vertical detachment from the anion ground state accesses this closed-shell singlet at an unstable geometry stretched far from its ground state.

In order to accurately describe the closed-shell singlet, triplet and open-shell singlet states of the reactive ring-open intermediate, EOM-EA, EOM-SF[88] and EOM-IP[79] calculations were carried out, all using the aug-cc-pVTZ basis set. First, the anion geometry was optimized by using the EOM-EA-CCSD method adopting the closed-shell singlet reference. This admittedly somewhat convoluted and unusual approach to anion geometry optimization resorted to, because direct CCSD optimization of the anion using Hartree-Fock (HF) orbitals exhibited significant spin-contamination, $\langle S^2 \rangle \approx 1.0$, or convergence problems. For the EOM-EA-CCSD optimized anion geometry, the high-spin ($M_S = 1$)

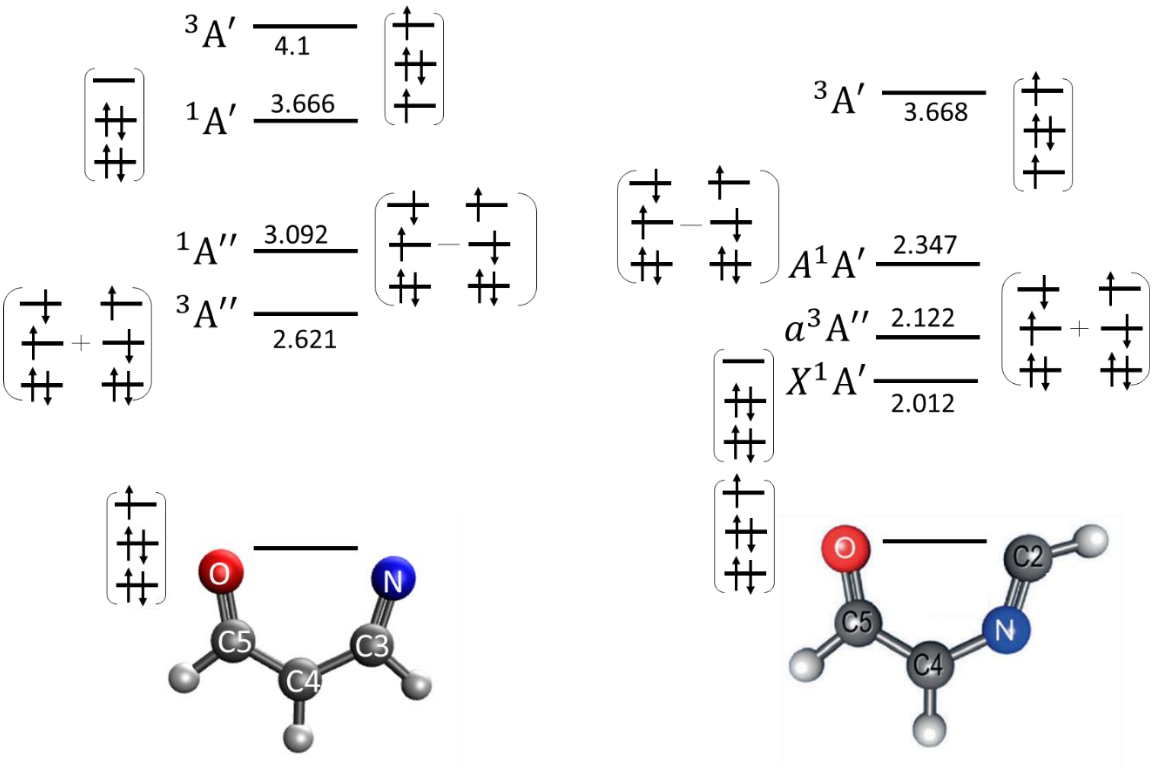

Figure 5.4 The electronic structures of ring-opened isoxazole and oxazole. The electron configurations of each state are labeled. The neutral states determined from EOM-XX-CCSD/aug-cc-pVTZ, XX=IP, SF calculations are given in electron volts relative to the corresponding optimized anion geometry.

component of the neutral triplet state, $^3\text{A}''$:…$(15\text{a}')^2(3a'')^1(16a')^1$, hereafter referred to as the "triplet reference", was accessed by removal of a $3a''$ electron from the anion, $X\,^2\text{A}'$:…$(15\text{a}')^2(3a'')^2(16a')^1$. The closed-shell singlet, $^1\text{A}'$:…$(15\text{a}')^2(3a'')^2(16a')^0$, and the open-shell singlet $^1\text{A}''$:…$(15\text{a}')^2(3a'')^1(16a')^1$ states were accessed by single spin-flip excitations from the $\text{M}_\text{S} = 1$ triplet reference. The $\text{M}_\text{S} = 0$ component of the triplet was used to calculate the singlet-triplet energy gaps.

As already mentioned, the use of HF orbitals for open-shell states of this system indicated significant spin contamination. In each of these calculations the expectation value of the spin-squared operator is given. Theoretically this should give S(S+1) where S is the total spin of the molecule. When this result is off by more than 10% the results are said to be spin contaminated and the energy values cannot be trusted. This can be solved by using unrestricted B3LYP orbitals for the calculations, because coupled-cluster theory methods are relatively insensitive to the choice of orbital basis. A summary of the neutral state energies is displayed in Figure 5.4, with all numeric values given relative to the anion equilibrium geometry.

A comparison with the states of ring-opened oxazole is given in Figure 5.4. Of particular note is that the lowest energy transition for isoxazole is the triplet $^3\text{A}''$ followed by the open-shell singlet $^1\text{A}''$ and a much higher energy closed shell singlet $^1\text{A}'$. Neutral ring-opened oxazole has all three of these corresponding states at nearly the same energy and the closed shell singlet is the lowest in energy.

The agreement of the theoretical spectrum, marked by the red line in Figure 5.3, and the experimental spectra is quite remarkable. The transition energies of the lowest two neutral states are predicted within ~0.1 eV. We assign the $^3\text{A}''$ to be the lowest energy vertical transition from the anion with a VDE of 2.64(1) eV. The open shell singlet $^1\mathrm{A}''$ is assigned to the peak with VDE = 2.95(2). The closed-shell singlet and the open-shell triplet cannot be unambiguously assigned from the experimental spectra but are in agreement with the EOM-SF calculations given in Figure 5.4.

5.5 Conclusion

The addition of an electron to isoxazole dissociates the O-N bond and upon photodetachment leaves a diradical. The through-space interaction of these radical centers gives several closely lying electronic states at very strained geometries. Backed by theoretical analysis, the experiment has provided a snapshot of this reactive intermediate.

CHAPTER 6: SUMMARY AND FUTURE DIRECTIONS

6.1 Summary

In this dissertation, we have explored applications of photoelectron imaging spectroscopy. The systems we have studied have served to broaden our understanding of electronic structure. Specifically, we expanded the model used to predict photoelectron angular distributions for hybridized molecules, probed bond dissociations and molecular stabilities of radical systems. This work has used the power of photoelectron imaging and the analysis of photoelectron angular distributions to gain insight into the complexity of electronic structure and explore the chemistry of elusive and reactive molecular structures.

6.2 Experiments with Preliminary Data

6.2.1 Ring Opening of Furan

During a study on the aromaticity of furanide,[64] the mass spectrum showed the presence of a species with a mass of 68 amu (Figure 6.1). The sample in use at the time was furan with argon as a carrier gas. Argon is an inert gas and unlikely to produce any ions in the gas phase. Furan has a mass of 68 amu and thus is the most logical assignment for this peak. A photoelectron image was collected at 306 nm and is displayed in Figure 6.2 alongside its corresponding energy spectrum. Just as was seen with ring-opening in oxazole and isoxazole the spectrum is broad and congested, with what appears to be 2 close lying electronic states.

Geometry optimization calculations were performed using the Qchem 4.0[69] software package. Upon optimization of the anion, the O-C bond was cleaved, and the ring opened slightly. This is similar to the cases of oxazole and isoxazole described in Chapter 5. Equation-of-motion (EOM)[79] ionization potential calculations predicted states at 1.59 eV and 1.99 eV, neither of which are apparent in the energy spectrum. However, these calculations had large spin contamination with $S^2 > 1.00$, which for a doublet should be S^2~ .75. The techniques used to reduce spin contamination described in Chapters 4 and 5 were not known to the author at the time.

Shortly after the spectrum at 306 nm was collected the ion signal disappeared. The sample holder was dry and new furan sample was added. However, the conditions to make furan anion were not able to be recreated. The ion signal seen in Figure 6.1 is barely large enough to image. Attempts were made to heat the sample, and backing pressures were varied from ~1 atm to ~3 atm. Many adjustments to electron gun/cannon settings were not able to achieve sufficient ion generation.

6.2.2 Tetrahydrofuran

The mass spectrum in Figure 6.1 shows a large peak at a mass of 72 amu. This peak was consistently larger than either furanide or furan. A photoelectron image was taken at 532 nm and is displayed in Figure 6.3 alongside its corresponding energy spectrum (a). With a mass of 72 amu for neutral furan seeded in argon there are not many possibilities. The photoelectron image clearly does not correspond to photodetachment from O_2^- solvated by argon which would have well resolved vibrational resolution. It was suspected that mass 72 could be the hydrogenated tetrahydrofuran (THF) despite the unlikely chemistry that would need to occur in its formation. While H_2^+ abstraction is not uncommon in the ion generation conditions of the source chamber, the insertion of H_2^+ is significantly less likely.

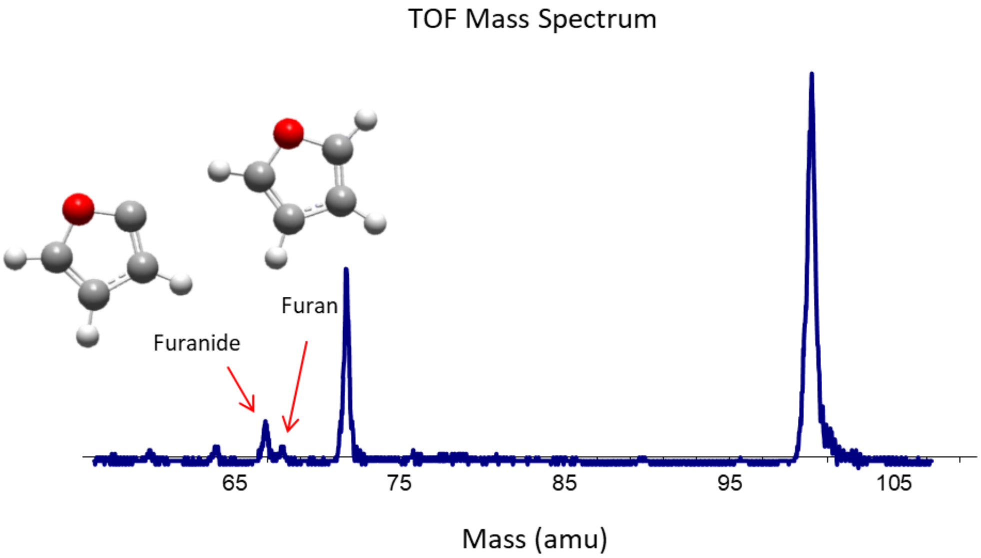

Figure 6.1 Time-of-flight mass spectrum of furan with argon as a carrier gas. Note the relative size of the ion intensities.

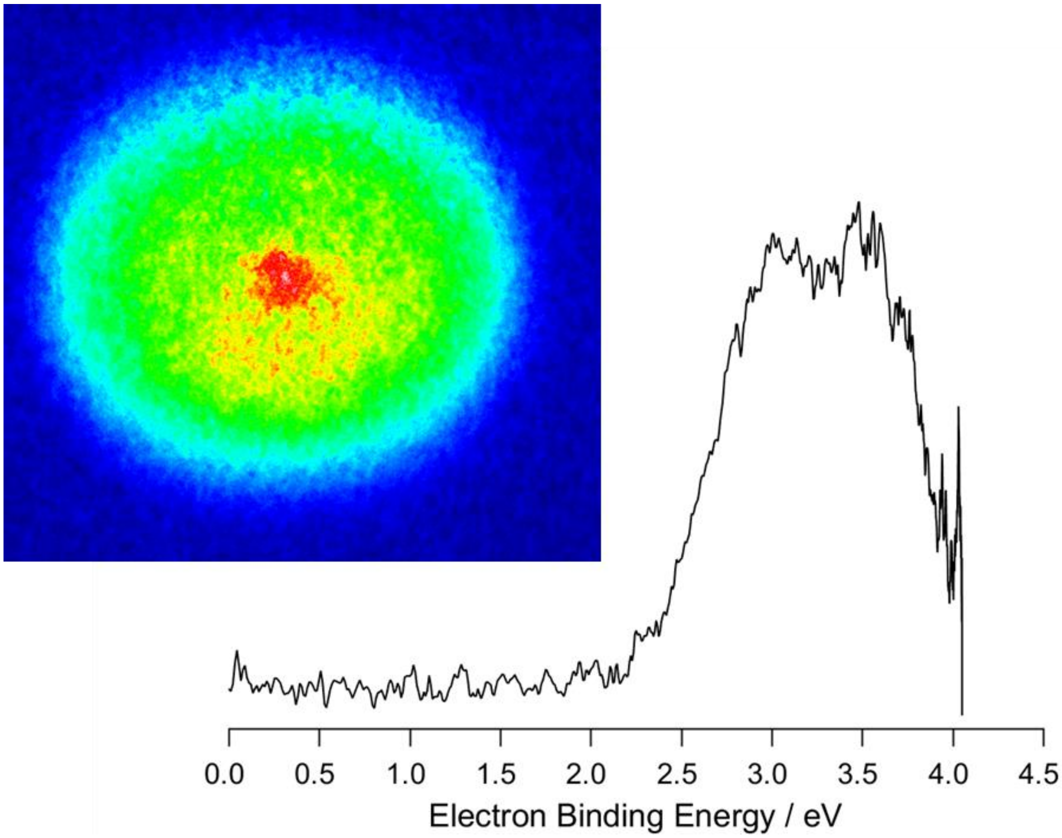

Figure 6.2 Photoelectron image and the corresponding spectrum of m/z 68 collected at 306 nm.

The sample holder was emptied, and vacuum pumped to remove furan and tetrahydrofuran was inserted into the sample holder. A photoelectron image was collected at 532 nm and the corresponding photoelectron spectrum is given in figure 6.3(b). The spectra of m/z 72 from the furan and THF sources are nearly identical. This strongly suggests convergent chemistry from the two sources and a THF anion is a possibility. However, THF is a strong solvent and in the process of making this measurement the O-ring in the nozzle was dissolved and significant damage was done to the nozzle. O-rings that will not dissolve in THF are expensive and this project was shelved to pursue other ideas. If the project is returned to, furan should be used as the source of m/z 72.

6.3 Ideas for Future Studies

In this section, I outline several projects related to work presented in this dissertation that could improve our understanding of electronic structure and the modeling of PADs.

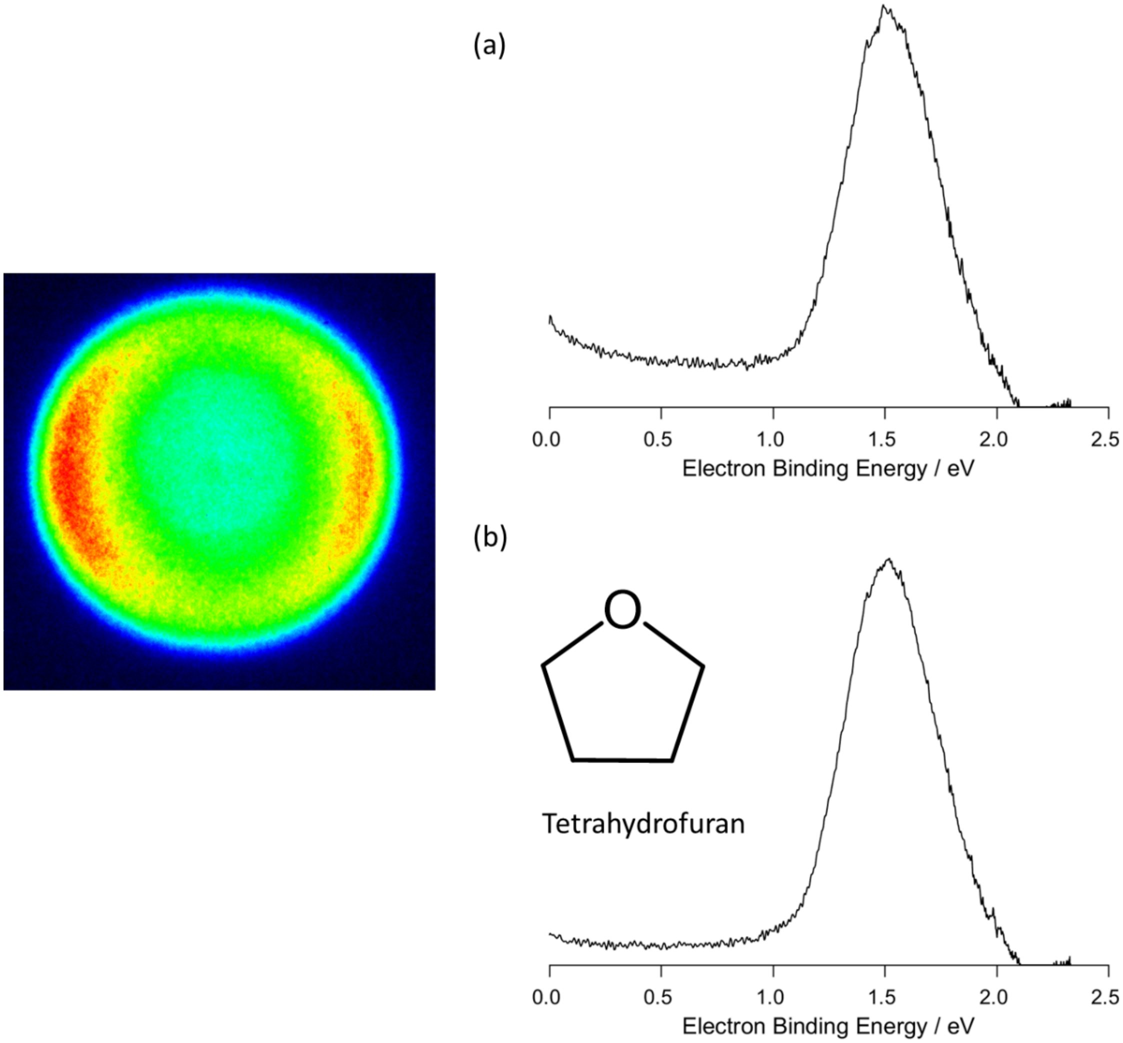

Figure 6.3 Photoelectron image and corresponding energy spectrum (a) of m/z = 72 with furan as the source. (b) photoelectron spectrum of m/z = 72 with tetrahydrofuran as the source.

6.3.1 Deprotonation Induced Ring-Opening

In chapter 4 we explored the different isomers created upon deprotonation of isoxazole. Deprotonation of isoxazole at the C3- position broke the oxygen nitrogen bond and opened the ring structure. Calculations have been performed[75] to show that a similar behavior is exhibited by two other heterocyclic aromatics, isothiazole and isoselenezole. These structures are shown in Scheme 6.1. These deprotonated anions have not been studied experimentally and would provide insight into the structural changes that occur with hetroatom substitution. Pyrazole is also of interest in this study as initial calculations indicate[75] that the N-N bond remains intact upon C3- deprotonation. This contrast can give us insight into the aromaticity and stability of these structures.

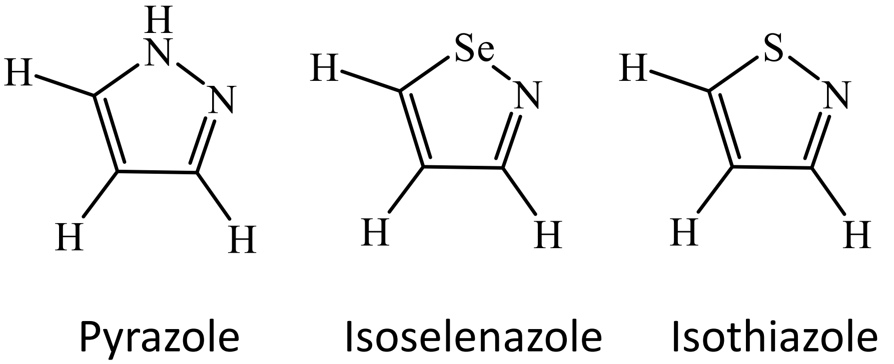

Scheme (6.1)

6.3.2 Trends in Heterocyclic Aromatic Anions

In chapter 3 we expanded on the s-p mixing model and explored the relationship between *ab initio* calculated Hirshfeld charges and the diffuse tails of the anionic wavefunctions. There are many heterocyclic aromatics that could be studied to solidify this relationship. Several of the heteroatoms could be replaced by the less electronegative atoms selenium or nitrogen, yielding selenophene, pyrrole, pyrazole, selenazole, and imidazole (Figure 6.4). According to our predictions in Chapter 3, the less electronegative selenium would have a smaller electron withdrawing effect than either sulfur or oxygen. This would lead to a smaller local Hirshfeld charge. Each of these molecules could be studied computationally before the experiments were performed to predict how they would fall into the trends outlined in Chapter 3.

Additionally, the only 6-member heterocyclic aromatic studied this way was pyridinide[34]. The relatively weak electron withdrawing groups near the deprotonation site lead to an anionic orbital that was very similar in spatial extent to atomic carbon. Substituting the nitrogen for oxygen or sulfur would allow us to compare the differences of the s-p mixing model between five- and six-membered rings. The additional atoms would likely withdraw more of the electron density and lead to a smaller local Hirshfeld charge[68].

The substitution of carbons in pyridinide for various heteroatoms would allow for the study of the impact on the s-p mixing model of symmetry breaking. It is not clear if symmetry breaking in these heterocyclic aromatics has an impact on the s-p mixing model. Six-member rings offer more ways to examine the effects of individual heteroatom substitutions.

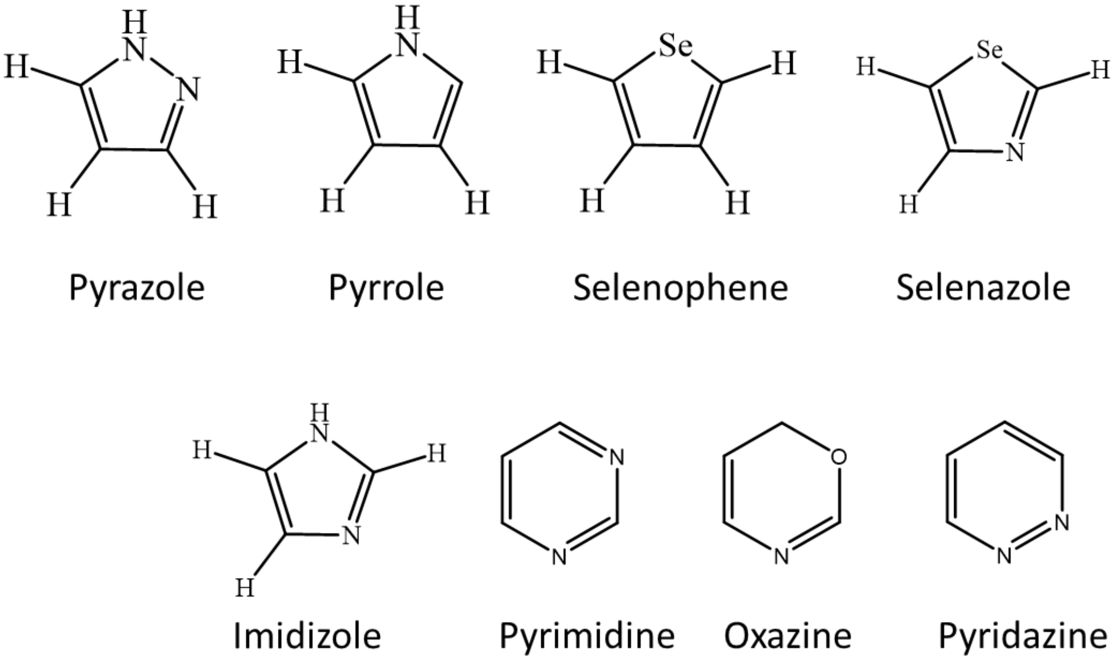

Figure 6.4 Heterocyclic aromatic molecules suggested for future photoelectron imaging studies.

APPENDEX A: BETACALC

This is the MATLAB code for the BetaCalc program. I will explain the basic use and a few details that are often adjusted directly in the code based on the needs of the user. BetaCalc finds the values of the anisotropy parameter, beta, for each peak specified by the user. It can analyze any number of files for the same molecule simultaneously. Add the polar.dat and speed.dat files that are obtained from the BASEX[49] software to a directory in the same folder as betacalc.m. BetaCalc starts by asking you to choose the directory of all your files. Only polar.dat and speed.dat files will be read. You will then be asked how many peaks you wish to analyze. The maximum number of peaks currently allowed is 15, but in the unlikely event you want to analyze more you can change the number 15 in `numpeaks>15` on line 63. You will then be shown the radial distribution and asked to give the radius of these peaks one at a time. Beta will then be calculated for each peak you specified in the first file.

The peak you specified can be used exactly or BetaCalc can check for a higher point within a few radial units. The calculation will start some specified number of radial units away from the peak. Line 77 defines the maximum up to 2 radial units away. If you want to exactly define the radius of the peak, then comment out lines 77 and 79 and uncomment line 80.

Rmin and Rmax define the starting points over which beta is determined. If the peak is sharp and narrow, then 10-15 is usually sufficient. If the peak is broad or you are slicing it into pieces, then you can consider much larger or smaller numbers.

numSteps defines how many beta values you will calculate and thus average over. The default is 5, but this can be adjusted.

After BetaCalc has finished determining beta for the first file, (assuming there are more than one) you will be asked if the radius is the same in each subsequent file. If you are analyzing several images for the same molecule saying yes will allow BetaCalc to determine beta for the same peaks you already specified for each file.

The values of beta are stored in a variable named beta_# where # is based on the order the files were analyzed. This order is printed to the command line for easy reference.

BetaCalc:

```
clear;clc;close all;clear all;

fprintf(1,'Pick the directory and this will find beta for all peaks in
all polar.dat files in it\n');
directories=dir;%get files
Nf=length(directories);%number of files
redefine = -1;
numpeaks=-1;
index(30)=0;
ind=0;
for i=3:Nf
    if directories(i).isdir
       ind=ind+1;
       filename=directories(i).name;
       fprintf(1,'%d: %s\n',ind,filename);
       index(ind)=i;
    end
end
ipick=1000;

while ipick>ind || ipick<=0
    ipick=input('\nEnter number> ');
end
if ipick>0
    dirname=directories(index(ipick)).name;
end

fprintf(1,'\nYou are using: %s\n\n',dirname);

files=dir(dirname);
Nf=length(files);
num_files=0;
```

```
for n=3:Nf       %find all files with the extension polar.dat and store
the names
                filename=files(n).name;
                lf=length(filename);
                if lf > 8
                    if strcmp(filename(lf-8:lf),'polar.dat')
                        num_files=num_files+1;
                        fname=[dirname,'/',filename];
                        farr{num_files}=fname;
                        fprintf(1,'%d: %s\n',num_files,filename);

                    end
                end
end
for Fileindex = 1:length(farr)
    currentFile = char(farr(Fileindex));
    polar = load(currentFile);
    theta = polar(1:160,2);
    radians=theta*pi/180;

    speedFile = [currentFile(1:length(currentFile)-9),'speed.dat'];
    speed = load(speedFile); %load the speed file corresponding to the
current polar file
    figure
    plot(speed(:,1),speed(:,2))
    fprintf(1,'You are using: %s\n',char(farr(Fileindex)));
    if Fileindex > 1
        while redefine > 1 || redefine <0
            redefine = input('Are the number of peaks and peak
locations the same as before? (1 for yes 0 for no)');
        end
    end
    if redefine < 1
        while numpeaks>15 || numpeaks<=0
            numpeaks=input('\nEnter number of peaks> ');
        end
        peakloc=zeros(1,numpeaks);
        for index=1:numpeaks
            peakloc(1,index)=input('Enter the radius of the peaks one
at a time:');
        end
        redefine = -1;
    end

     numSteps=5;
     eval(['beta_' num2str(Fileindex) ' = zeros(numSteps,numpeaks);'])
    for currentPeak = 1:numpeaks
        tempPeakCh = find(speed(:,1)==peakloc(currentPeak)); %find the
peak closest to the value input by user
        [~,peakCh] = max(speed(tempPeakCh-2:tempPeakCh+2,2)); %finds
the
%         max amplitude close to the location specified.
        peakCh=peakCh+tempPeakCh-3;
%         peakCh = tempPeakCh;
        %begin BETACALC
```

```
        Rmin = speed(peakCh-15,1); %number of steps away from the peak
        Rmax= speed(peakCh+15,1);
        width=Rmax-Rmin;
        Itheta=zeros(160,1);

        for step =1:numSteps
            for thetaindex =1:160
                polarindex = find(polar(:,2)==theta(thetaindex));
                for n = 0:2*width
                    Itheta(thetaindex,1) = Itheta(thetaindex,1) +
polar(polarindex(polar(polarindex)==Rmin+.5*n),3);
                end
            end
            ft = fittype( 'a*(1+beta/2*(3*cos(x)^2-1))', 'independent',
'x', 'dependent', 'y' );
            opts = fitoptions( ft );
            opts.Display = 'Off';
            opts.Lower = [-Inf -Inf];
            opts.StartPoint = [0.970592781760616 0.957166948242946];
            opts.Upper = [Inf Inf];

            % Fit model to data.
            [fitresult, gof] = fit(radians,Itheta(:,1), ft, opts );
            temp = coeffvalues(fitresult);
            eval(['beta_' num2str(Fileindex) '(step,currentPeak) =
temp(2);'])
            Rmin = Rmin-.5;
            Rmax=Rmax+.5;
            width=Rmax-Rmin;
        end
    end
end
```

REFERENCES

1. Minkin, V. I.; Glukhovtsev, M. N.; Simkin, B. Y. *Aromaticity and Antiaromaticity: Electronic and Structural Aspects*; Wiley: New York, 1994.

2. Krygowski, T. M.; Cyranski, M. K.; Czarnocki, Z.; Hafelinger, G.; Katritzky, A. R., "Aromaticity: A theoretical concept of immense practical importance", *Tetrahedron* 56, 1783-1796 (2000).

3. Lipshutz, B. H., "5-Membered Heteroaromatic Rings as Intermediates in Organic-Synthesis", *Chem. Rev.* 86, 795-819 (1986).

4. Bruinsma, O. S. L.; Geertsma, R. S.; Bank, P.; Moulijn, J. A., "Gas-Phase Pyrolysis of Coal-Related Aromatic-Compounds in a Coiled Tube Flow Reactor .1. Benzene and Derivatives", *Fuel* 67, 327-333 (1988).

5. Zhu, J.; Mo, J.; Lin, H. Z.; Chen, Y.; Sun, H. P., "The recent progress of isoxazole in medicinal chemistry", *Biorg. Med. Chem.* 26, 3065-3075 (2018).

6. Lamberth, C., "Oxazole and Isoxazole Chemistry in Crop Protection", *J. Heterocycl. Chem.* 55, 2035-2045 (2018).

7. Turchi, I. J.; Dewar, M. J. S., "Chemistry of Oxazoles", *Chem. Rev.* 75, 389-437 (1975).

8. Kasai, P. H.; Mcleod, D., "Electron-Spin Resonance Study of Heterocycles. 2. Pyrrole, Pyrazole, Imidazole, and Indole Anion Radicals", *J. Am. Chem. Soc.* 95, 27-31 (1973).

9. Sysak, A.; Obminska-Mrukowicz, B., "Isoxazole ring as a useful scaffold in a search for new therapeutic agents", *Eur. J. Med. Chem.* 137, 292-309 (2017).

10. Ichino, T.; Andrews, D. H.; Rathbone, G. J.; Misaizu, F.; Calvi, R. M. D.; Wren, S. W.; Kato, S.; Bierbaum, V. M.; Lineberger, W. C., "Ion chemistry of 1H-1,2,3-Triazole", *J. Phys. Chem. B* 112, 545-557 (2008).

11. Adams, G. W.; Bowie, J. H.; Hayes, R. N., "Negative-Ion Fragmentations of Deprotonated Heterocycles. The Isothiazole, Thiazole, Isoxazole, and Oxazole Ring-Systems", *Int. J. Mass Spectrom.* 114, 163-182 (1992).

12. Einstein, A., "Heuristic viewpoint on the production and conversion of light", *Ann. Physik* 17, 132-148 (1905).

13. Ervin, K. M.; Lineberger, W. C., "Photoelectron Spectroscopy of Negative Ions", In *Advances in Gas Phase Ion Chemistry*; Adams, N. G., Babcock, L. M., Eds.; JAI Press: Greenwich, 1992; Vol. 1; pp 121-166.

14. Hanstorp, D.; Bengtsson, C.; Larson, D. J., "Angular distributions in photodetachment from O^-", *Phys. Rev. A* 40, 670-675 (1989).

15. Reid, K. L., "Photoelectron angular distributions", *Annu. Rev. Phys. Chem.* 54, 397-424 (2003).

16. Sanov, A., "Laboratory-Frame Photoelectron Angular Distributions in Anion Photodetachment: Insight into Electronic Structure and Intermolecular Interactions", *Annu. Rev. Phys. Chem.* 65, 341-363 (2014).

17. Chandler, D. W.; Houston, P. L., "Two-Dimensional Imaging of State-Selected Photodissociation Products Detected by Multiphoton Ionization", *J. Chem. Phys.* 87, 1445-1447 (1987).

18. Parker, D. H.; Eppink, A. T. J. B., "Photoelectron and Photofragment Velocity Map Imaging of State-Selected Molecular-Oxygen Dissociation/Ionization Dynamics", *J. Chem. Phys.* 107, 2357-2362 (1997).

19. Eppink, A. T. J. B.; Parker, D. H., "Velocity map imaging of ions and electrons using electrostatic lenses: Application in photoelectron and photofragment ion imaging of molecular oxygen", *Rev. Sci. Instrum.* 68, 3477-3484 (1997).

20. Alconcel, L. S.; Deyerl, H. J.; Continetti, R. E., "Effects of alkyl substitution on the energetics of enolate anions and radicals", *J. Am. Chem. Soc.* 123, 12675 (2001).

21. Surber, E.; Sanov, A., "Photoelectron imaging spectroscopy of molecular and cluster anions: CS_2^- and $OCS^-(H_2O)_{1,2}$", *J. Chem. Phys.* 116, 5921-5924 (2002).

22. Grumbling, E. R.; Sanov, A., "Photoelectron angular distributions in negative-ion photodetachment from mixed s–p states", *J. Chem. Phys.* 135, 164302 (2011).

23. Khuseynov, D.; Blackstone, C. C.; Culberson, L. M.; Sanov, A., "Photoelectron angular distributions for states of any mixed character: An experiment-friendly model for atomic, molecular, and cluster anions", *J. Chem. Phys.* 141, 124312 (2014).

24. Zare, R. N., "Photoejection Dynamics", *Mol. Photochem.* 4, 1-37 (1972).

25. Bethe, H. A.; Salpeter, E. E. *Quantum Mechanics of One- and Two-Electron Atoms*; Springer-Verlag; Academic Press Inc.: Berlin; New York, 1957.

26. Cooper, J.; Zare, R. N., "Angular Distributions in Atomic Anion Photodetachment", *J. Chem. Phys.* 48, 942-943 (1968).

27. Cooper, J.; Zare, R. N., "Angular Distributions in Atomic Anion Photodetachment (Erratum)", *J. Chem. Phys.* 49, 4252 (1968).

28. Wigner, E. P., "On the behavior of cross sections near thresholds", *Phys. Rev.* 73, 1002-1009 (1948).

29. Fano; Dill, D., "Angular Momentum Transfer in the Theory of Angular Distributions", *Phys. Rev. A* 6, 185-192 (1972).

30. Reed, K. J.; Zimmerman, A. H.; Andersen, H. C.; Brauman, J. I., "Cross sections for photodetachment of electrons from negative ions near threshold", *J. Chem. Phys.* 64, 1368-1375 (1976).

31. Akin, F. A.; Schirra, L. K.; Sanov, A., "Photoelectron imaging study of the effect of monohydration on O_2^- photodetachment", *J. Phys. Chem. A* 110, 8031-8036 (2006).

32. Van Duzor, M.; Mbaiwa, F.; Wei, J.; Singh, T.; Mabbs, R.; Sanov, A.; Cavanagh, S. J.; Gibson, S. T.; Lewis, B. R.; Gascooke, J. R., "Vibronic coupling in the superoxide

anion: The vibrational dependence of the photoelectron angular distribution", *J. Chem. Phys.* 133, 174311 (2010).

33. Grumbling, E. R.; Sanov, A., "Solvation effects on angular distributions in $H^-(NH_3)_n$ and $NH_2^-(NH_3)_n$ photodetachment: Role of solute electronic structure", *J. Chem. Phys.* 135, 164301 (2011).

34. Culberson, L. M.; Blackstone, C. C.; Sanov, A., "Photoelectron Angular Distributions of Pyridinide: A Benchmark Application of the Mixed s-p Model to a Truly Polyatomic Anion", *J. Phys. Chem. A* 117, 11760-11765 (2013).

35. Culberson, L. M.; Blackstone, C. C.; Wallace, A. A.; Sanov, A., "Aromatic Stabilization and Hybridization Trends in Photoelectron Imaging of Heterocyclic Radicals and Anions", *J. Phys. Chem. A* 119, 9770-9777 (2015).

36. Sanov, A.; Grumbling, E. R.; Goebbert, D. J.; Culberson, L. M., "Photodetachment anisotropy for mixed s-p orbitals: 8/3 and other fractions", *J. Chem. Phys.* 138, 054311 (2013).

37. Mabbs, R.; Surber, E.; Sanov, A., "Photoelectron Imaging of Negative Ions: Atomic Anions to Molecular Clusters", *Analyst* 128, 765-772 (2003).

38. Velarde, L. Ph.D. dissertation, University of Arizona, 2008.

39. Wiley, W. C.; McLaren, I. H., "Time-of-Flight Mass Spectrometer with Improved Resolution", *Rev. Sci. Instrum.* 26, 1150 (1955).

40. Surber, E.; Ananthavel, S. P.; Sanov, A., "Nonexistent electron affinity of OCS and the stabilization of carbonyl sulfide anions by gas phase hydration", *J. Chem. Phys.* 116, 1920-1929 (2002).

41. Alconcel, L. S.; Deyerl, H. J.; DeClue, M.; Continetti, R. E., "Dissociation dynamics and stability of cyclic alkoxy radicals and alkoxide anions", *J. Am. Chem. Soc.* 123, 3125-3132 (2001).

42. Johnson, M. A.; Lineberger, W. C., "Pulsed Methods for Cluster Ion Spectroscopy", In *Techniques for the Study of Ion Molecule Reactions*; Farrar, J.M., Saunders, W.H., Eds.; Wiley: New York, 1988; pp 591-635.

43. Klots, C. E., "Evaporative cooling", *J. Chem. Phys.* 83, 5854 (1985).

44. Klots, C. E.; Compton, R. N., "Electron-Attachment to Vanderwaals Polymers of Carbon-Dioxide and Nitrous-Oxide", *J. Chem. Phys.* 69, 1636-1643 (1978).

45. Alexander, M. L.; Levinger, N. E.; Johnson, M. A.; Ray, D.; Lineberger, W. C., "Recombination of Br_2^- photodissociated within mass selected ionic clusters", *J. Chem. Phys.* 88, 6200-10 (1988).

46. Johnson, M. A.; Alexander, M. L.; Lineberger, W. C., "Photodestruction cross sections for mass-selected ion clusters: $(CO_2)_n^+$", *Chem. Phys. Lett.* 112, 285-290 (1984).

47. Bordas, C.; Paulig, F.; Helm, H.; Huestis, D. L., "Photoelectron imaging spectrometry: Principle and inversion method", *Rev. Sci. Instrum.* 67, 2257-2268 (1996).

48. Pichugin, K. Ph.D. dissertation, University of Arizona, 2010.

49. Dribinski, V.; Ossadtchi, A.; Mandelshtam, V. A.; Reisler, H., "Reconstruction of abel-transformable images: The Gaussian basis-set expansion abel transform method", *Rev. Sci. Instrum.* 73, 2634-2642 (2002).

50. Heck, A. J. R.; Chandler, D. W., "Imaging Techniques For the Study of Chemical Reaction Dynamics", *Annu. Rev. Phys. Chem.* 46, 335-372 (1995).

51. Cooper, J.; Zare, R. N., "Photoelectron angular distributions", In *Atomic collision processes*; Geltman, S., Mahanthappa, K. T., Brittin, W. E., Eds.; Gordon and Breach, Science Publishers: New York, London, Paris, 1968; Vol. XI-C; pp 317-337.

52. Seideman, T., "Time-resolved photoelectron angular distributions as a means of studying polyatomic nonadiabatic dynamics", *J. Chem. Phys.* 113, 1677-1680 (2000).

53. Landau, L. D.; Lifshitz, E. M. *Quantum Mechanics: Nonrelativistic Theory*; 3rd ed. ed.; Pergamon Press: Oxford, 1977.

54. Cohen-Tannoudji, C.; Diu, B.; Laloë, F. *Quantum Mechanics*; John Wiley & Sons: New York, London, Sydney, Toronto, 1977; Vol. 2.

55. Lineberger, W. C.; Hotop, H.; Patterson, T. A., "Photodetachment Threshold Processes", In *Electron and Photon Interactions with Atoms*; Kleinpoppen, H., McDowell, M. R. C., Eds.; Plenum Publishing Corporation: New York, 1976; pp 125-132.

56. Mead, R. D.; Lykke, K. R.; Lineberger, W. C., "Photodetachment Threshold Laws", In *Electronic and Atomic Collisions*; Eichler, J., Hertel, I. V., Stolterfoht, N., Eds.; Elsevier, 1984; pp 721-730.

57. Oana, C. M.; Krylov, A. I., "Cross sections and photoelectron angular distributions in photodetachment from negative ions using equation-of-motion coupled-cluster Dyson orbitals", *J. Chem. Phys.* 131, 124114 (2009).

58. Slater, J. C., "Atomic shielding constants", *Phys. Rev.* 36, 57-64 (1930).

59. Cavanagh, S. J.; Gibson, S. T.; Gale, M. N.; Dedman, C. J.; Roberts, E. H.; Lewis, B. R., "High-resolution velocity-map-imaging photoelectron spectroscopy of the O^- photodetachment fine-structure transitions", *Phys. Rev. A* 76, 052708 (2007).

60. Grumbling, E. R.; Pichugin, K.; Velarde, L.; Sanov, A., "Further evidence for resonant photoelectron-solvent scattering in nitrous oxide cluster anions", *J. Phys. Chem. A* 114, 1367-1373 (2010).

61. Hall, J. L.; Siegel, M. W., "Angular Dependence of Laser Photodetachment of Negative Ions of Carbon, Oxygen, and Hydrogen", *J. Chem. Phys.* 48, 943-945 (1968).

62. Breyer, F.; Frey, P.; Hotop, H., "High-Resolution Photoelectron Spectrometry of Negative-Ions - Fine-Structure Transitions in O- and S- Photodetachment", *Z. Phys. A: Hadrons Nucl.* 286, 133-138 (1978).

63. Brandon, W. D.; Lee, D. H.; Hanstorp, D.; Pegg, D. J., "Photodetachment of the C- ion", *J. Phys. B* 31, 751-760 (1998).

64. Culberson, L. M.; Sanov, A., "Electronic states of thiophenyl and furanyl radicals and dissociation energy of thiophene via photoelectron imaging of negative ions", *J. Chem. Phys.* 134, 204306 (2011).

65. Culberson, L. M.; Blackstone, C. C.; Wysocki, R.; Sanov, A., "Selective deprotonation of oxazole and photoelectron imaging of the oxazolide anion", *Phys. Chem. Chem. Phys.* 16, 527-532 (2014).

66. Mulliken, R. S., "Electronic Population Analysis on LCAO-MO Molecular Wave Functions. I." *J. Chem. Phys.* 23, 1833-1840 (1955).

67. Wiberg, K. B.; Rablen, P. R., "Atomic Charges", *J. Org. Chem.* 83, 15463-15469 (2018).

68. Hirshfeld, F. L., "Bonded-Atom Fragments for Describing Molecular Charge-Densities", *Theoretica Chimica Acta* 44, 129-138 (1977).

69. Shao, Y. H.; Gan, Z. T.; Epifanovsky, E.; Gilbert, A. T. B.; Wormit, M.; Kussmann, J.; Lange, A. W.; Behn, A.; Deng, J.; Feng, X. T.; Ghosh, D.; Goldey, M.; Horn, P. R.; Jacobson, L. D.; Kaliman, I.; Khaliullin, R. Z.; Kus, T.; Landau, A.; Liu, J.; Proynov, E. I.; Rhee, Y. M.; Richard, R. M.; Rohrdanz, M. A.; Steele, R. P.; Sundstrom, E. J.; Woodcock, H. L.; Zimmerman, P. M.; Zuev, D.; Albrecht, B.; Alguire, E.; Austin, B.; Beran, G. J. O.; Bernard, Y. A.; Berquist, E.; Brandhorst, K.; Bravaya, K. B.; Brown, S. T.; Casanova, D.; Chang, C. M.; Chen, Y. Q.; Chien, S. H.; Closser, K. D.; Crittenden, D. L.; Diedenhofen, M.; DiStasio, R. A.; Do, H.; Dutoi, A. D.; Edgar, R. G.; Fatehi, S.; Fusti-Molnar, L.; Ghysels, A.; Golubeva-Zadorozhnaya, A.; Gomes, J.; Hanson-Heine, M. W. D.; Harbach, P. H. P.; Hauser, A. W.; Hohenstein, E. G.; Holden, Z. C.; Jagau, T. C.; Ji, H. J.; Kaduk, B.; Khistyaev, K.; Kim, J.; Kim, J.; King, R. A.; Klunzinger, P.; Kosenkov, D.; Kowalczyk, T.; Krauter, C. M.; Lao, K. U.; Laurent, A. D.; Lawler, K. V.; Levchenko, S. V.; Lin, C. Y.; Liu, F.; Livshits, E.; Lochan, R. C.; Luenser, A.; Manohar, P.; Manzer, S. F.; Mao, S. P.; Mardirossian, N.; Marenich, A. V.; Maurer, S. A.; Mayhall, N. J.; Neuscamman, E.; Oana, C. M.; Olivares-Amaya, R.; O'Neill, D. P.; Parkhill, J. A.; Perrine, T. M.; Peverati, R.; Prociuk, A.; Rehn, D. R.; Rosta, E.; Russ, N. J.; Sharada, S. M.; Sharma, S.; Small, D. W.; Sodt, A., "Advances in molecular quantum chemistry contained in the Q-Chem 4 program package", *Mol. Phys.* 113, 184-215 (2015).

70. Frisch, M. J.; Trucks, G. W.; Schlegel, H. B.; Scuseria, G. E.; Robb, M. A.; Cheeseman, J. R.; Scalmani, G.; Barone, V.; Mennucci, B.; Petersson, G. A.; Nakatsuji, H.; Caricato, M.; Li, X.; Hratchian, H. P.; Izmaylov, A. F.; Bloino, J.; Zheng, G.; Sonnenberg, J. L.; Hada, M.; Ehara, M.; Toyota, K.; Fukuda, R.; Hasegawa, J.; Ishida, M.; Nakajima, T.; Honda, Y.; Kitao, O.; Nakai, H.; Vreven, T.; Montgomery, J., J. A.; Peralta,

J. E.; Ogliaro, F.; Bearpark, M.; Heyd, J. J.; Brothers, E.; Kudin, K. N.; Staroverov, V. N.; Kobayashi, R.; Normand, J.; Raghavachari, K.; Rendell, A.; Burant, J. C.; Iyengar, S. S.; Tomasi, J.; Cossi, M.; Rega, N.; Millam, N. J.; Klene, M.; Knox, J. E.; Cross, J. B.; Bakken, V.; Adamo, C.; Jaramillo, J.; Gomperts, R.; Stratmann, R. E.; Yazyev, O.; Austin, A. J.; Cammi, R.; Pomelli, C.; Ochterski, J. W.; Martin, R. L.; Morokuma, K.; Zakrzewski, V. G.; Voth, G. A.; Salvador, P.; Dannenberg, J. J.; Dapprich, S.; Daniels, A. D.; Farkas, Ö.; Foresman, J. B.; Ortiz, J. V.; Cioslowski, J.; Fox, D. J.; Revision A.1 ed.Gaussian, Inc.: Wallingford, CT, 2009.

71. Kobayashi, T.; Kubota, T.; Ezumi, K.; Utsunomiya, C., "Photoelectron Angular-Distribution Study of Some Isoxazoles Combined with Perturbation Theoretic Approach", *Bull. Chem. Soc. Jpn.* 55, 3915-3919 (1982).

72. Modelli, A.; Burrow, P. D., "Electron attachment to the aza-derivatives of furan, pyrrole, and thiophene", *J. Phys. Chem. A* 108, 5721-5726 (2004).

73. Palmer, M. H.; Findlay, R. H.; Egdell, R. G., "Electronic-Structure of Heteroaromatic Molecules: Ab Initio Calculations and Photoelectron Spectra for Isomeric Oxazoles and Some Isomeric Oxadiazoles", *J. Mol. Struct.* 40, 191-210 (1977).

74. Cole, C. A.; Demarais, N. J.; Yang, Z. B.; Snow, T. P.; Bierbaum, V. M., "Heterocyclic Anions of Astrobiological Interest", *Astrophys. J.* 779 (2013).

75. Kaur, D.; Khanna, S.; Kaur, R. P., "The role of conjugative interactions in acidic and basic character of five membered aromatic heterocyclics", *J. Mol. Struct.* 949, 14 - 22 (2010).

76. Velarde, L.; Habteyes, T.; Sanov, A., "Photodetachment and photofragmentation pathways in the $[(CO_2)_2(H_2O)_m]^-$ cluster anions", *J. Chem. Phys.* 125, 114303 (2006).

77. Lee, J.; Grabowski, J. J., "Reactions of the Atomic Oxygen Radical-Anion and the Synthesis of Organic Reactive Intermediates", *Chem. Rev.* 92, 1611-1647 (1992).

78. Shao, Y.; Molnar, L. F.; Jung, Y.; Kussmann, J.; Ochsenfeld, C.; Brown, S. T.; Gilbert, A. T. B.; Slipchenko, L. V.; Levchenko, S. V.; O'Neill, D. P.; DiStasio, R. A.; Lochan, R. C.; Wang, T.; Beran, G. J. O.; Besley, N. A.; Herbert, J. M.; Lin, C. Y.; Van Voorhis, T.; Chien, S. H.; Sodt, A.; Steele, R. P.; Rassolov, V. A.; Maslen, P. E.; Korambath, P. P.; Adamson, R. D.; Austin, B.; Baker, J.; Byrd, E. F. C.; Dachsel, H.; Doerksen, R. J.; Dreuw, A.; Dunietz, B. D.; Dutoi, A. D.; Furlani, T. R.; Gwaltney, S. R.; Heyden, A.; Hirata, S.; Hsu, C. P.; Kedziora, G.; Khalliulin, R. Z.; Klunzinger, P.; Lee, A. M.; Lee, M. S.; Liang, W.; Lotan, I.; Nair, N.; Peters, B.; Proynov, E. I.; Pieniazek, P. A.; Rhee, Y. M.; Ritchie, J.; Rosta, E.; Sherrill, C. D.; Simmonett, A. C.; Subotnik, J. E.; Woodcock, H. L.; Zhang, W.; Bell, A. T.; Chakraborty, A. K.; Chipman, D. M.; Keil, F. J.; Warshel, A.; Hehre, W. J.; Schaefer, H. F.; Kong, J.; Krylov, A. I.; Gill, P. M. W.; Head-Gordon, M., "Advances in methods and algorithms in a modern quantum chemistry program package", *Phys. Chem. Chem. Phys.* 8, 3172-3191 (2006).

79. Krylov, A. I., "Equation-of-motion coupled-cluster methods for open-shell and electronically excited species: The Hitchhiker's guide to Fock space", *Annu. Rev. Phys. Chem.* 59, 433-462 (2008).

80. Mabbs, R.; Mbaiwa, F.; Wei, J.; Van Duzor, M.; Gibson, S. T.; Cavanagh, S. J.; Lewis, B. R., "Observation of vibration-dependent electron anisotropy in O_2^- photodetachment", *Phys. Rev. A* 82, 011401 (2010).

81. Zoltewicz, J. A.; Deady, L. W., "Quaternization of Heteroaromatic Compounds: Quantitative Aspects", *Adv. Heterocycl. Chem.* 22, 71-121 (1978).

82. Khuseynov, D.; Dixon, A. R.; Goebbert, D. J.; Sanov, A., "Heterogeneous Substitution Effects in Chlorocyanomethyl Radical and Chlorocyanocarbene", *J. Phys. Chem. A* 117, 10681–10691 (2013).

83. Surber, E.; Sanov, A., "Imaging of Direct Photodetachment and Autodetachment of $(OCS)_2^-$: Excited-State Dynamics of the Covalent Dimer Anion", *Phys. Rev. Lett.* 90, 093001 (2003).

84. Salem, L.; Rowland, C., "Electronic Properties of Diradicals", *Angew. Chem. Int. Ed.* 11, 92-111 (1972).

85. Neumark, D. N., "Transition state spectroscopy", *Science* 272, 1446-1447 (1996).

86. Neumark, D. M., "Probing the transition state with negative ion photodetachment: experiment and theory", *Phys. Chem. Chem. Phys.* 7, 433-442 (2005).

87. Culberson, L. M.; Wallace, A. A.; Blackstone, C. C.; Khuseynov, D.; Sanov, A., "Spectroscopy of the breaking bond: the diradical intermediate of the ring opening in oxazole", *Phys. Chem. Chem. Phys.* 16, 3964-3972 (2014).

88. Krylov, A. I., "Spin-flip configuration interaction: an electronic structure model that is both variational and size-consistent", *Chem. Phys. Lett.* 350, 522-530 (2001).

89. Levchenko, S. V.; Krylov, A. I., "Equation-of-motion spin-flip coupled-cluster model with single and double substitutions: Theory and application to cyclobutadiene", *J. Chem. Phys.* 120, 175-185 (2004).